Climate Dynamics
https://doi.org/10.1007/s00382-020-05474-1

The semi-diurnal cycle of deep convective systems over Eastern China and its surrounding seas in summer based on an automatic tracking algorithm

Wenwen Li[1] · Feng Zhang[2,3] · Yueyue Yu[1] · Hironobu Iwabuchi[4] · Zhongping Shen[5] · Guoyin Wang[2] · Yijun Zhang[2]

Received: 24 November 2019 / Accepted: 2 October 2020

Abstract
Deep convective systems (DCSs) are associated with severe weather events and can affect regional and global climate. To study the semi-diurnal variation of DCSs over Eastern China and its surrounding seas in summer, we modified the Tracking of Organized Convection Algorithm through a 3-D segmentatioN (TOOCAN) by employing Himawari-8 operational cloud property (CLP) products instead of original infrared images, and renamed the algorithm as TOOCAN-CLP. The DCSs detected over land and sea are divided into small-, medium-, and large-sized classes based on the convective core equivalent radius. The small and medium-sized DCSs over land exhibit a maximum occurrence in the afternoon, which is associated with local thermal instability and sea breeze circulation. The occurrence of small DCSs over the tropical sea areas varies analogously to that of small continental DCSs but with a smaller amplitude. However, medium-sized DCSs over the sea, which account for the majority of DCSs over the sea, exhibit weak semi-diurnal variability. Large DCSs over inland China and its surrounding seas tend to initiate at night and decay in the daytime. The generation of large DCSs over inland China at night is mainly due to the enhanced transport of warm and moist air by strong large-scale prevailing southerly or southwesterly winds, while the large offshore DCSs accompanied by heavy rainfall is closely associated with the interaction between local offshore breeze and large-scale monsoon flows, as well as gravity waves.

Keywords Deep convective system · TOOCAN-CLP algorithm · Semi-diurnal cycle · Cloud top height · Cloud optical thickness

1 Introduction

A deep convective system (DCS) is a contiguous cold cloud shield which is composed of three elements: a deep convective core where intense precipitation occurs, a stratiform anvil with a more uniform texture of lighter precipitation, and a connected nonprecipitating cirrus canopy (Houze Jr 2004). DCSs are widely known for their associated local extreme weather events, including flooding, lightning, strong wind, and even hail. Moreover, DCSs are essential for weather and climate processes worldwide because they can link convective systems to large-scale and synoptic-scale systems such as monsoons and tropical waves (Okamura et al. 2017; Payne and Mcgarry 1977), which strongly influence energy and water cycles as well as cloud radiative forcing and feedback (Roca et al. 2010).

Observations from polar-orbiting satellites and geostationary satellites make it feasible to capture the properties of DCSs consistently and continuously at both regional

✉ Feng Zhang
fengzhang@fudan.edu.cn

1 Key Laboratory of Meteorological Disaster, Ministry of Education, Nanjing University of Information Science and Technology, Nanjing, China

2 Department of Atmospheric and Oceanic Sciences and Institute of Atmospheric Sciences, Fudan University, Shanghai 200438, China

3 Shanghai Qi Zhi Institute, Shanghai 200232, China

4 Center for Atmospheric and Oceanic Studies, Graduate School of Science, Tohoku University, Sendai, Japan

5 Shanghai Ecological Forecasting and Remote Sensing Center, Shanghai, China

Published online: 17 October 2020

and global scales (Chen et al. 2019a; Kikuchi and Suzuki 2019; Masunaga 2013; Phadtare and Bhat 2019; Sieglaff et al. 2013). Satellite-based studies of convective clouds and rainfall have shown prominent diurnal patterns in their variabilities (Byon and Lim 2005; Chen and Houze 1997a; Garreaud and Wallace 1997; Mao and Wu 2012; Nitta and Sekine 1994; Sui et al. 1997; Yang et al. 2006). The majority of these studies found that the peak in convection and rainfall tends to appear in the early morning over the sea but in the late afternoon or early evening over land. However, Mcgarry and Reed (1978) and Wexler (1983) argued that there is also an afternoon maximum in rainfall and convection over the sea. Furthermore, Albright et al. (1985) found that the time of maximum coverage of cold clouds over the sea varies dramatically with the brightness temperature (BT) threshold employed in the analysis. Specifically, they found that, in the South Pacific convergence zone, deep clouds with tops colder than 218 K reached their maximum areal extent around sunrise, while clouds with tops colder than 237 K exhibited a different behavior, with a pronounced maximum of coverage in the afternoon and evening. Based on a combined visible–infrared threshold method, Fu et al. (1990) discovered a time lag between the diurnal cycle of the coverage of deep convective clouds and the associated cirrus anvil clouds over the tropic pacific region, namely, deep convection peaks in the early morning and a maximum in the cirrus anvil clouds occurs 9–12 h later.

The mechanism of the diurnal cycle of convective activities has been investigated in numerous studies. Over land and along coastlines, the main factors strongly influencing the diurnal cycle of convection and precipitation include the thermal properties of the underlying surface and the local circulation caused by the thermodynamic difference among terrain types (Chen and Takahashi 1995). Yang and Slingo (2000) found that a diurnal signal over land can be propagated to the surrounding seas via gravity waves. Due to the much larger thermal inertia of the sea surface, the role of the thermal condition of the sea surface in initiating convections is less significant than that of the land surface (Huang et al. 2018; Putri et al. 2017). Nevertheless, Chen and Houze (1997a) state that in the afternoon, the solar radiation on the sea surface and the overlying atmospheric boundary layer becomes strong enough to offer a favorable condition for the formation and growth of convection. They also mention that the life cycle of convection is an additional factor that affects the diurnal cycle of DCSs. Examples of this are convective systems in the vicinity of Borneo, which initiate in the middle of the night during the winter monsoon as offshore land breeze interacts with the monsoonal northeasterly winds. As a result, the maximum coverage of cold clouds often occurs in the morning, which is not simultaneous with the formation of deep convection (Houze et al. 1981).

Despite strenuous research efforts in monitoring and forecasting of DCSs in recent decades, the detailed characteristics of various convective activities (e.g., with different areal extents or with different surface types), especially their diurnal variation contrasts, still remain unclear due to the crude and unreliable methods used for the detection and tracking of DCSs. Such uncertainty in the representation of the diurnal cycle of DCSs could have a remarkable effect on the cloud radiative forcing and feedback in climate models. The effective and continuous identification and tracking of DCSs are conducive to investigating the features of various DCSs. This would help us obtain a comprehensive understanding of the diurnal variation of convective activities.

In previous studies, the signature of BTs at the infrared window channel, usually centered at 11 μm, has been used to identify DCSs from satellite images using a wide variation of temperature thresholds from 208 to 253 K (Chen and Houze 1997b; Mapes and Houze Jr 1993; Williams and Houze 1987). Inoue et al. (2009) identify the DCSs in terms of cloud types based on a split window. Utilizing the BT difference (BTD) between 11 and 12 μm band (split window), the algorithm can classify the optically thick cumulus cloud and the thinner cirrus cloud type, which is more physically motivated than using the single-band BT threshold method. But strictly speaking, the choice of the BTD threshold for a wide area is too difficult, since BTD is not only determined by the cloud optical thickness but also influenced by the atmospheric profile and surface condition. More recently, some hybrid classification algorithms were developed to identify DCSs based on a synthesis of ground-based scanning radar or multiple polar-orbiting satellite observations (Feng et al. 2011; Liu et al. 2008; Yuan and Houze Jr 2010). Intuitively, these methods may be limited by the difficulty of instantaneously acquiring DCS features covering a wide range of areas.

Successively tracking each targeted convective cluster is a great challenge since the morphological parameters of a DCS vary rapidly over its life cycle. Numerous automatic tracking methods have been designed, such as the area-overlapping method (Williams and Houze 1987), an algorithm to minimize the cost function that measures the coherence in direction and speed of features between convective clusters in successive images (Hodges and Thorncroft 1997), a centroid tracking algorithm (Johnson et al. 1998), the maximum spatial correlation tracking algorithm (Carvalho and Jones 2001), and an algorithm to track and analyze convective clouds in diverse datasets (Heikenfeld et al. 2019). In the area-overlapping method, which is the most widely used, two cloud elements in two consecutive frames are considered as the same system if the area overlap exceeds 50% or 10,000 km^2. However, this method fails to yield a stable and smooth lifestyle of DCSs and suffers from splitting and merging events. Furthermore, this method

is inapplicable to small and fast-moving DCSs when using satellite data with low temporal and spatial resolutions. A fully automatic method, namely the Tracking of Organized Convection Algorithm through a 3-D segmentatioN (TOOCAN), was proposed to deal with the problem due to the splitting and merging of events (Fiolleau and Roca 2013). TOOCAN detects a DCS starting from its convective core, which has a lower brightness temperature, progressing to its connected cloud shield, which has a higher brightness temperature, by iteratively applying a temperature interval in a three-dimensional spatiotemporal space. To track DCSs, the "Grab 'em, Tag 'em, Graph 'em" (GTG) method developed by Whitehall et al. (2014) utilizes a graph that is constructed with cloud elements acting as graph nodes linked by weighting edges based on the overlapping magnitude. Most recently, Huang et al. (2018) developed an algorithm by applying the Kalman filter to the traditional area-overlapping method. This algorithm can effectively track small-sized and rapidly moving convection by estimating the direction and speed of the objective convection and predicting the position of potential DCSs and is feasible for use with low-resolution satellite images. All of these tracking algorithms were developed based on the brightness temperature from satellite images but the detection of transmissive clouds (optically thin cirrus clouds) in the infrared window channel is difficult because the cloud radiative temperature observed by satellite instruments may be higher than the air temperature at the same altitude (Wylie and Woolf 2000). Additionally, brightness temperature, which has no direct relation to cloud thickness or underlying surface precipitation, cannot be used to separate the convective core and anvil clouds in a DCS (Rickenbach 1998). Contrarily, cloud optical thickness can assist in identifying the convective core, which has similar cloud top temperatures to the surrounding anvil cloud shield but thicker clouds and stronger precipitation (Ronald et al. 2016). Therefore, the inclusion of cloud properties such as cloud top height (CTH) and cloud optical thickness (COT) is conducive to improving the detection and tracking of DCSs. In this paper, the TOOCAN algorithm was modified by employing Himawari-8/Advanced Himawari Imager (H-8/AHI) level-2 operational cloud property (CLP) products instead of original brightness temperature, and the algorithm was renamed as TOOCAN-CLP. We employ this modified method to study the semi-diurnal cycle of DCSs over Eastern China and its surrounding seas in summer.

This article is constructed as follows. Section 2 introduces the dataset and the TOOCAN-CLP algorithm. Section 3 exhibits the semi-diurnal variation of DCSs of different sizes and associated precipitation as well as the specific location of their occurrence over land and sea. In Sect. 4, we discuss the underlying physical processes that give rise to the semi-diurnal variation of DCSs of different sizes. The conclusion is presented in Sect. 5.

2 Data and methods

2.1 Data description

We conduct this study in the summertime (June, July, and August) from 2016 to 2018 over Eastern China and its surrounding seas. The study region is located between 5° N and 40° N latitude and between 101° E and 139° E longitude as shown in Fig. 1.

2.1.1 H-8/AHI level-2 operational cloud products

H-8/AHI level-2 operational cloud products with a temporal resolution of 10 min and a spatial resolution of 0.05° × 0.05° were provided by the P-Tree System, Japan Aerospace Exploration Agency (JAXA). The cloud properties, including cloud effective radius, cloud optical thickness, and cloud top height, are retrieved from visible (VIS) and near-infrared (NIR) bands of H-8/AHI. The retrieval technique called the "Comprehensive Analysis Program for Cloud Optical Measurement" (CAPCOM-INV), proposed by Nakajima and Nakajma (1995) and Kawamoto et al. (2001), was applied to retrieve the water cloud properties. The optical properties of the water clouds were obtained based on the Lorenz–Mie theory. The CAPCOM-INV algorithm was advanced (CAPCOM-INV-ice) to retrieve the radiative properties of ice clouds using the Voronoi light-scattering model (Ishimoto et al. 2012). The retrieval of cloud optical thickness may be influenced by the three-dimensional effect of clouds at a large solar zenith angle (Loeb and Davies 1996). Therefore, the cloud properties are only available at solar zenith angles below 80°. Several studies have validated the AHI retrieval products and demonstrated its adequate performance. Lai et al. (2019) systematically compared AHI retrieval products with Moderate Resolution Imaging Spectroradiometer (MODIS) cloud products and demonstrated the reliability of AHI retrieval products. Letu et al. (2018) proved the ability of AHI ice cloud products to monitor the cloud properties of deep convective clouds. Moreover, the AHI cloud mask products were investigated and validated against Cloud-Aerosol Lidar and Infrared Pathfinder Satellite Observation (CALIPSO) measurements then used to examine the semi-diurnal variations of cloud cover over the Tibetan Plateau by Shang et al. (2018).

2.1.2 GPM satellite precipitation products

The satellite precipitation products used in this paper is from the global precipitation measurement (GPM) constellation satellite mission, which is an international network of satellites that supplies global observations of rain and snow.

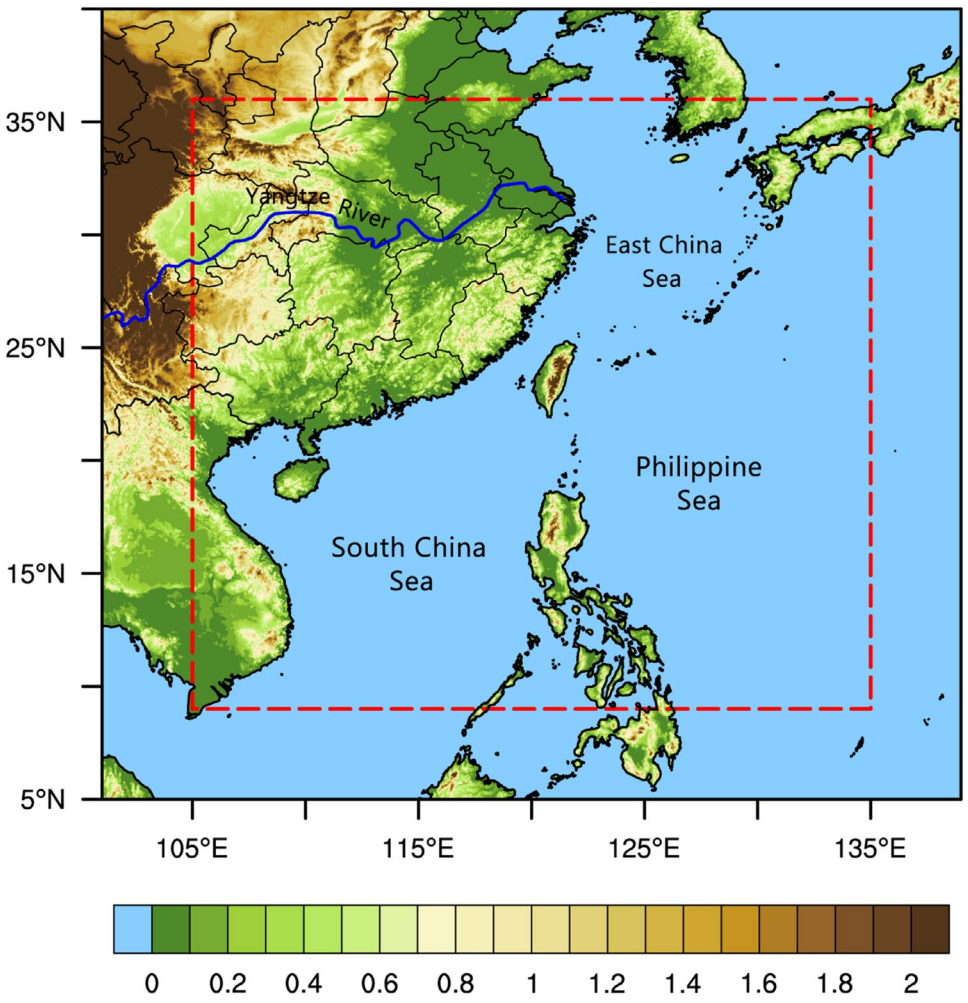

Fig. 1 Map of the study region. The shaded color shows the topography (km) from GTOPO30, a global digital elevation model (DEM) supplied by the US Geological Survey (USGS) with a horizontal resolution of 30 arc seconds. The blue line indicates the Yangtze River, and the red dashed rectangle outlines the area 4° away from the boundary of the study region

The enhanced sensitivity of the dual-frequency precipitation radar (DPR) and the high-frequency bands on the GPM Microwave Imager (GMI) qualify GPM to enhance the ability to estimate light rain and falling snow as well as heavy rainfall. The Integrated Multi-satellitE Retrievals for GPM (IMERG) is the unified US algorithm employed to generate multi-satellite precipitation products for the GPM team. The IMERG product with a $0.1° \times 0.1°$ spatial resolution over the domain 60° N–S is computed from satellite microwave precipitation estimates, combined with microwave-calibrated infrared (IR) satellite estimates, revised with monthly surface precipitation-gauge data (Huffman et al. 2018). In this paper, the Level 3 IMERG Final Half Hourly $0.1° \times 0.1°$ (GPM_3IMERGHH) in version 05 is chosen for the analysis of precipitation associated with convection due to its high temporal and spatial resolution.

2.1.3 JRA-55 atmospheric reanalysis data

To investigate the variation of the underlying surface thermal properties and large-scale circulation relevant to DCS development, the Japanese 55-year Reanalysis (JRA-55) is used in this study. JRA-55 is the second Japanese global atmospheric reanalysis provided by the Japan Meteorological Agency (JMA). The dataset has a temporal resolution of 6 h and a spatial resolution of $1.25° \times 1.25°$. Detailed information about JRA-55 data can be found in Kobayashi et al. (2015). Chen et al. (2014) confirmed the superior quality of JRA-55 data in representing the warm-season diurnal cycle over East Asia by comparing it with recent mainstream reanalysis [e.g., Interim European Centre for Medium-Range Weather Forecasts (ECMWF) Re-Analysis (ERA-Interim), Modern-Era Retrospective Analysis for Research and Applications (MERRA)]. JRA-55 data has been widely used to study the synoptic features and environmental conditions for various rainfall events such as convective afternoon rainfall, nocturnal long-duration rainfall, and typhoons (Akter and Ishikawa 2014; Chen et al. 2010; Huang et al. 2015; Putri et al. 2018; Zhou and Wu 2019). Particularly, Huang et al. (2015) demonstrated the capability of JRA-55 in depicting local sea–land breeze.

2.1.4 ERA5 atmospheric reanalysis data

Besides JRA-55, the fifth generation ECMWF atmospheric reanalysis (ERA5) is also used in this study to obtain the meteorological fields relevant to DCS development. The ERA5 reanalysis is produced using the Integrated Forecasting System (IFS cycle 41r2) with 4-D-Var data assimilation and covers the time period from January 1950 to present. ERA5 is prominent in its high temporal resolution of 1 h and spatial resolution of 0.25° × 0.25°. ERA5 is significantly improved compared to the ERA-Interim in various aspects, including better representation of tropical cyclones, better estimation of precipitation, and more accurate simulation of sea surface temperatures (Hennermann and Berrisford 2018). Furthermore, ERA5 has been applied in investigating convection environments in numerous studies (Czernecki et al. 2019; Ukkonen and Mäkelä 2019; Umakanth et al. 2019). More detailed descriptions of the ERA5 reanalysis can be found in Hersbach and Dee (2016).

2.2 DCS identification

To identify DCSs accurately and automatically, a simple definition of a DCS is introduced—that is, a high cloud shield which is composed of a convective core (CC) with severe precipitation, an associated stratiform region (SR), and a broad cirrus anvil (CA) (Fig. 2d). Many techniques that are used to extract the DCSs or separate CC, SR, and CA parts of DCSs are based on infrared brightness temperature thresholds, which suffer from large errors because brightness temperature has no direct relation to cloud thickness or underlying surface precipitation. However, combining brightness temperature and optical thickness has been found to improve the estimation of precipitation in DCSs (Stenz et al. 2016). Convective cores of DCSs are located where clouds are thicker than the ambient anvil cloud shield (Fig. 2d), and the inclusion of optical thickness is conducive to distinguishing these two regions with remarkably distinct thickness and precipitation intensity but similar brightness temperatures. Based on the above, in this study, DCSs are identified by combining the CTH with COT from H-8/AHI

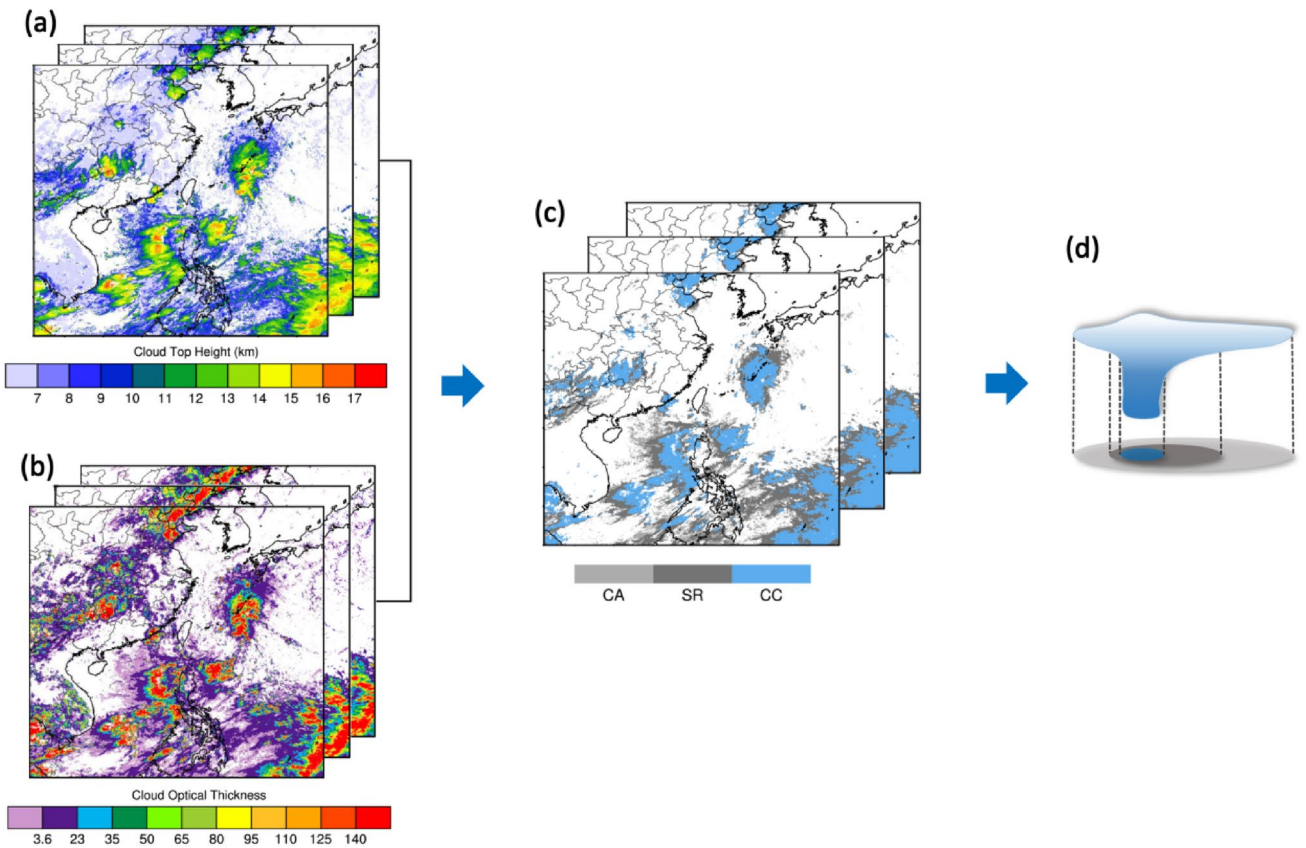

Fig. 2 Schematic of the deep convective system (DCS) identification method. The continuous cloud top height (CTH) (**a**) and cloud optical thickness (COT) (**b**) retrievals from Himawari-8/Advanced Himawari Imager (H-8/AHI) level-2 operational cloud products every 10 min. **c** The region of interest (ROI) for the convective core (CC), stratiform region (SR), and cirrus anvil (CA) according to the CTH and COT criteria. **d** The simple structure of the DCS; the cloud shaded in blue, dark gray, and light gray represents the CC, SR, and CA respectively

level-2 operational cloud products according to the International Satellite Cloud Climatology Project (ISCCP) cloud type classification (Rossow and Schiffer 1999) instead of single infrared brightness temperature thresholds as used in the original TOOCAN algorithm. ISCCP categorizes clouds into nine classes based on COT and cloud top pressure (CTP). Here, we use CTH, which can be a substitute for CTP. A CTH of 7 km is used as the threshold for extracting high clouds. The high clouds are further separated into cirrus, cirrostratus, and convective clouds according to COT, by using the COT boundaries at 3.6 and 23. Figure 2 illustrates how a potential DCS is identified. First, all pixels with a CTH greater than 7 km are extracted as the region of interest (ROI), and then the ROI is decomposed into CA, SR, and CC parts using the COT boundaries at 3.6 and 23 (Fig. 2c). Specifically, CC is extracted from the region where COT is greater than 23, and SR and CA, namely, cirrostratus and cirrus, are essentially a contiguous anvil cloud and are only split by COT threshold of 3.6.

Here, we present a comparison between cloud types from different classification and coincident observations from CALIPSO. Figure 3a shows a cloud type map defined by the AHI cloud products based on the cloud classification standard of ISCCP over 20° N–40° N and 100° W–140° W at 04:50 UTC on August 7, 2016 with CALIPSO orbit (red line). The cloud types along the orbit are given in Fig. 3b. Figure 3c exhibits the cloud types defined by the split windows algorithm, which is proposed by Purbantoro et al. (2018) based on different IR band combinations (12.4 μm and 13.3 μm band) of the Himawari-8 satellite. Figure 3d

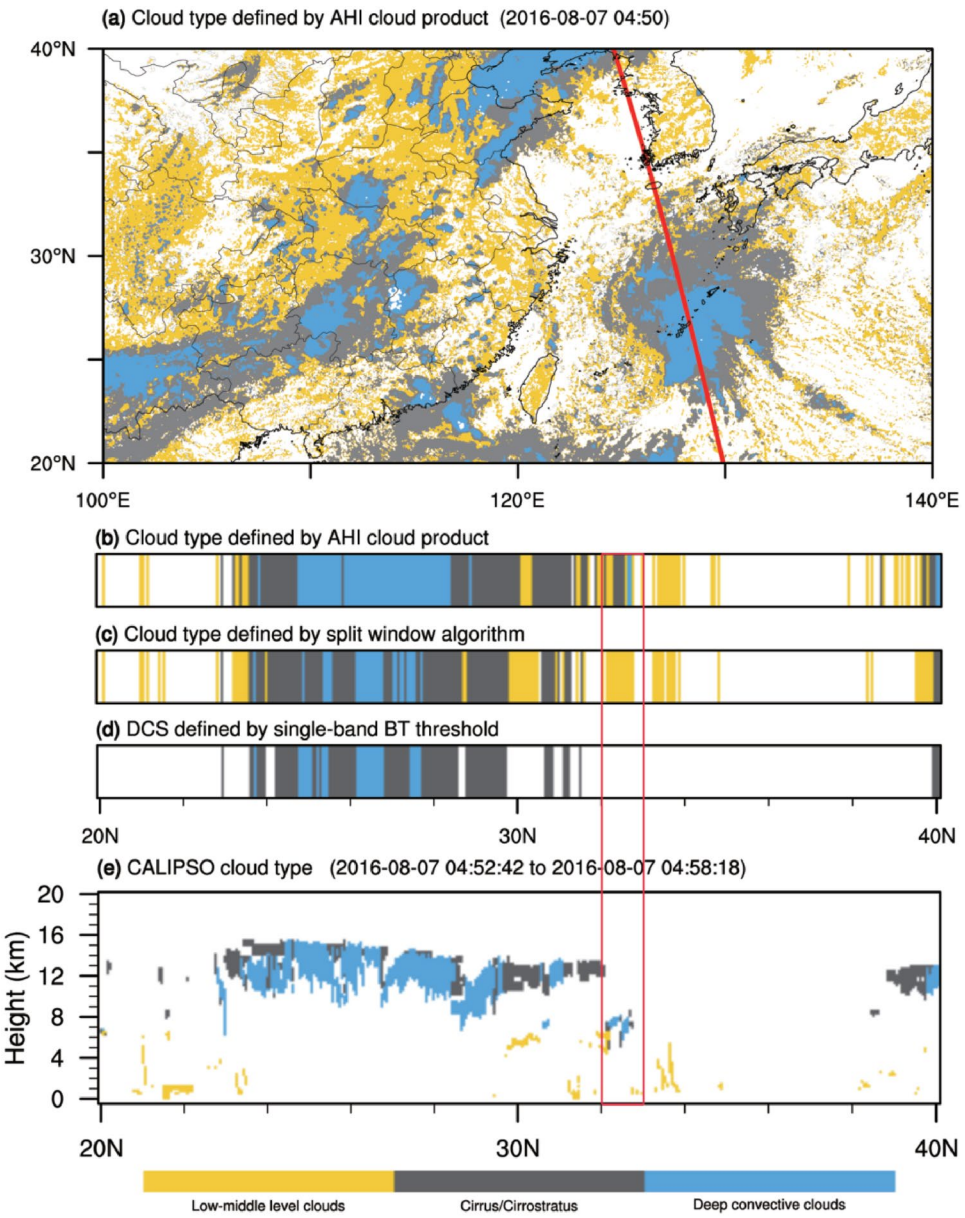

Fig. 3 Cloud type map from the AHI cloud products based on ISCCP at 04:50 UTC on August 7, 2016 over region (20° N–40° N, 100° W–140° W) with the CALIPSO orbit indicated by the red line (**a**). Cloud types defined by the AHI cloud products (**b**), cloud types defined by split window algorithm (**c**). DCS defined by single-band brightness temperature threshold (**d**) along the CALIPSO orbit. Vertical profile of cloud types from CALIPSO along the CALIPSO orbit (**e**). The red rectangle indicates the location of the convective clouds around 32.5° N, detected by CALIPSO and AHI cloud products

shows the cloud types using two BT thresholds: 223 K and 253 K. The 223 K threshold is employed to identify the convective region, namely the relatively active part of the DCSs (blue shade) (Barr-Kumarakulasinghe and Lwiza 1998; Feidas and Cartalis 2005; Meneguz et al. 2016). The 253 K threshold is chosen to delineate the warm boundary of the high level clouds associated with the convective region (gray shade) (Duvel 1989; Mapes and Houze Jr 1993). The vertical profile of cloud types from CALIPSO along the orbit is displayed in Fig. 3e. Compared with the cloud types from CALIPSO, cloud type classification by the AHI cloud products is capable of distinguishing the high clouds (cirrus, cirrostratus, and deep convective clouds) from the low and middle clouds, which is conducive to the extraction of DCS. However, some optically thinner clouds (cirrostratus or cirrus, around 29.5° N–32° N) surrounding the deep convective clouds are omitted or misjudged as low and middle clouds by the split window algorithm (Fig. 3c) and single-band BT threshold (Fig. 3d). Optically thin cirrus clouds tend to transmit terrestrial radiation, making observed brightness temperature warmer than the air temperature at the same altitude. Furthermore, thin high clouds may present similar cloud top BTs as thick low clouds in the satellite images. Therefore, it is difficult to use a threshold of brightness temperature to identify the thin cirrus clouds associated with DCS. In addition, the overall areal extent of the convective clouds identified by the AHI cloud products is larger than those derived from the other two methods, and closer to the observations from CALIPSO. Particularly, convective clouds with relatively low CTH around 32.5° N (highlighted by a red rectangle) are missed in Fig. 3c and d but are effectively detected in Fig. 3b, which proves the superior performance of cloud type classification by the AHI cloud products in detecting convective cores. Generally, this example demonstrates the validity of the cloud type classification by the AHI cloud products.

2.3 DCS tracking

The main idea of the TOOCAN algorithm is to detect DCSs starting from their convective cores, which are identified by a given brightness temperature, progressing to their associated anvil clouds, which have higher brightness temperatures, in a three-dimensional spatiotemporal space. This algorithm assumes that the COT of the cold cloud shield decreases away from the CC to the CA edges (Fig. 4b) (Ramanathan and Boer 1997). The spatiotemporal space, whose spatial axes are longitude and latitude, is assembled from a time sequence of the ROI generated by a combination of CTH and COT (Fig. 4a) at an interval of 10 min in the TOOCAN-CLP algorithm instead of the original satellite infrared data. The core of the tracking technique is the region-growing technique, which requires the generation of a few seeds (convective cores) to be grown as final DCSs in

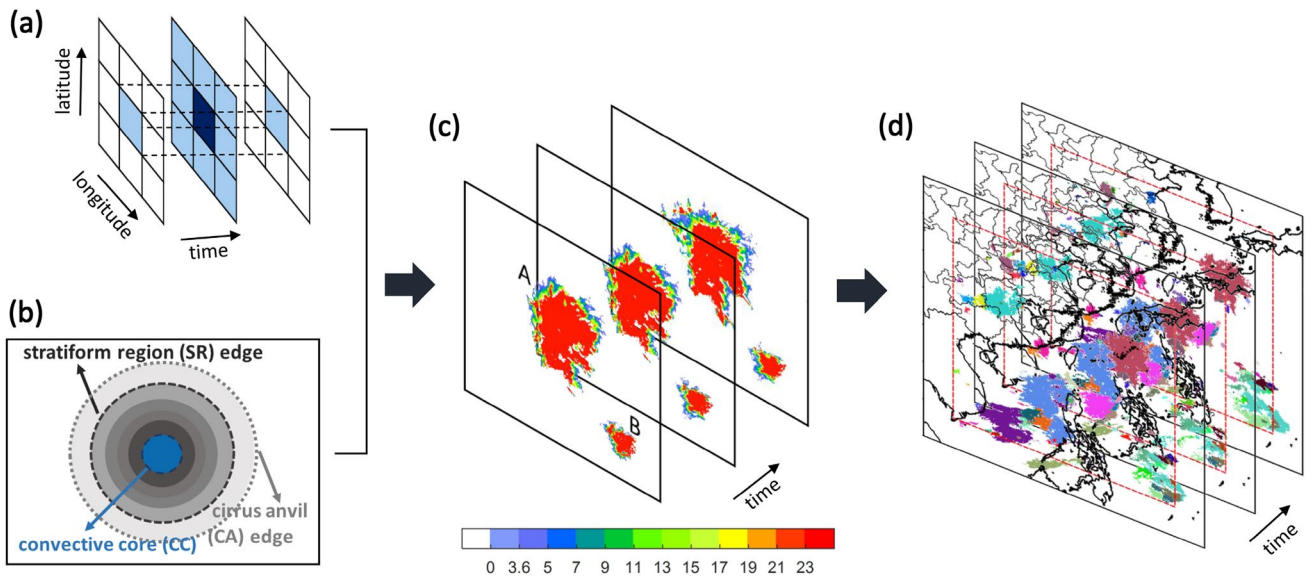

Fig. 4 Schematic of the DCS tracking. **a** Diagram of the ten-connected spatiotemporal neighborhood utilized for the region-growing: eight-connected spatial neighborhood and two-connected temporal neighborhood (past and future). **b** Exhibition of the projected DCS, where the optical thickness (gray shade) of the cold cloud shield decreases away from the convective core to the cold cloud shield edges. The blue part represents the CC, the dark gray dashed line depicts the SR edge, and the light gray dashed line depicts the CA edge. **c** The iterative process of the detection and growing of CCs by different COT thresholds in the three-dimensional spatiotemporal space. The shaded color represents the COT. **d** DCS segmentation using the TOOCAN-CLP algorithm. Different colors represent different DCSs

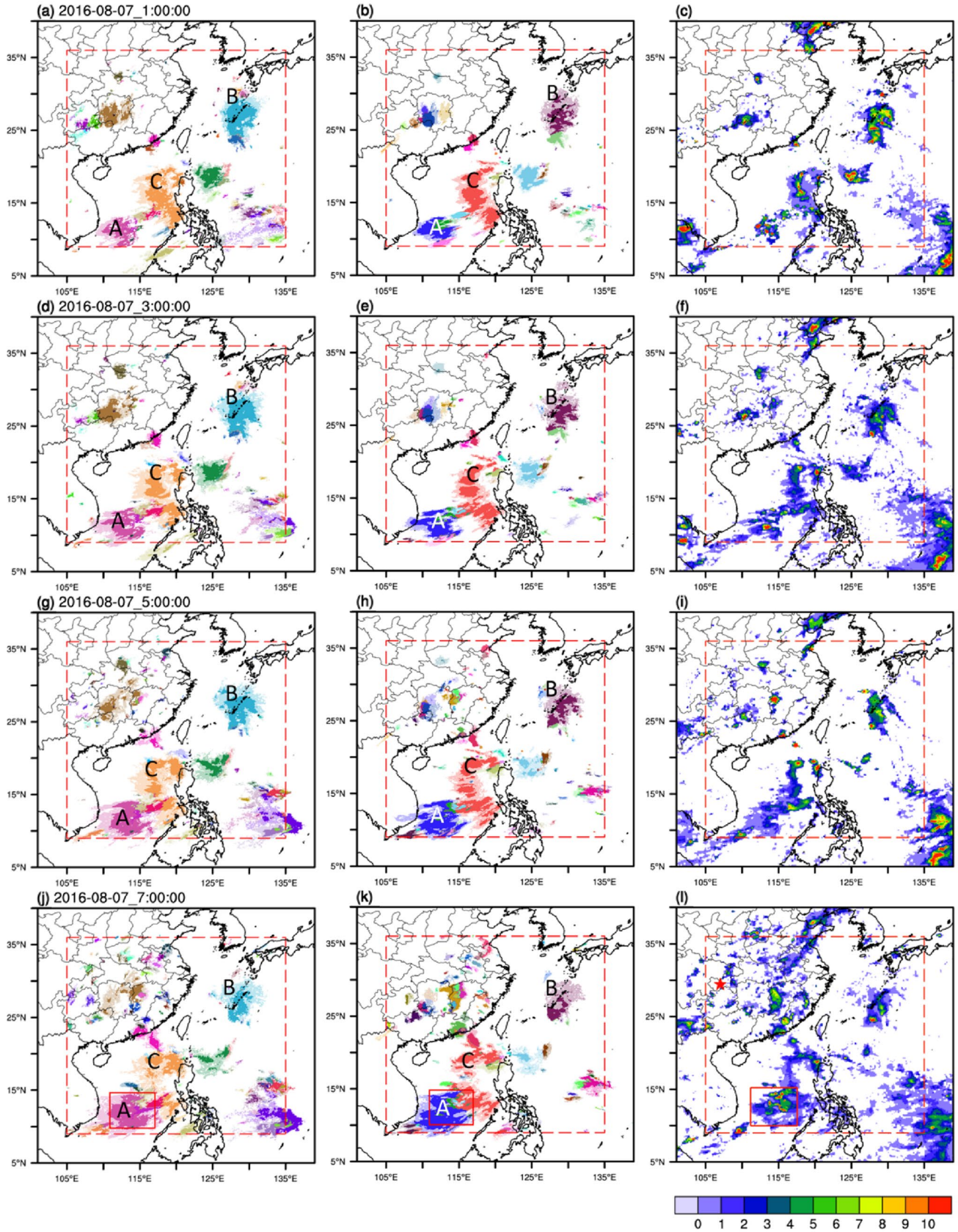
(a) 2016-08-07_1:00:00
(b)
(c)
(d) 2016-08-07_3:00:00
(e)
(f)
(g) 2016-08-07_5:00:00
(h)
(i)
(j) 2016-08-07_7:00:00
(k)
(l)
A
B
C
35°N
25°N
15°N
5°N
105°E
115°E
125°E
135°E
0 1 2 3 4 5 6 7 8 9 10

◂**Fig. 5** DCSs detected in the study region on August 7, 2016. The first and second columns show, respectively, DCS segmentation using the TOOCAN-CLP algorithm (**a**, **d**, **g**, **j**) and TOOCAN algorithm (**b**, **e**, **h**, **k**). Different colors represent different DCSs [dark colors represent CC, corresponding light colors represent entire anvil clouds (i.e., SR and CA)]. The third column shows the distributions of precipitation from GPM (mm h^{-1}) in the study region (**c**, **f**, **i**, **l**). The red star indicates the location of Chongqing Province

the spatiotemporal space (Meyer and Beucher 1990). A ten-connected spatiotemporal neighborhood, which is composed of eight spatial connections and two temporal connections (past and future) is employed for the region-growing process (Fig. 4a). First, the CCs are constructed in the spatiotemporal domain by detecting an unmarked contiguous set of pixels belonging to the ROI of the CC and assigning them labels. The newly detected CCs will be attached to a unique label and then the growing of the marked CCs to the cold cloud shield edge is based on an interactive process involving the application of multiple thresholds. The iterative process advances at a step of 2 ($\Delta COT = 2$), and is started to detect the intermediate cloud shield boundary over the ROI using a COT threshold of 21, and then of 19, 17, etc., is temporarily paused at the SR edge when the COT threshold reaches 3.6, and is finally stopped at the CA boundary with a COT value of 0 (Fig. 4c). The application of multiple thresholds is essential since the iterative process can effectively divide the DCSs and assign them individual labels, even when their anvil clouds are connected. As in the TOOCAN algorithm, the lifetime threshold, that is, the minimum duration allowed for the DCS to last, is set as 3 ROI frames under the detection step to exclude short-lived DCSs. The volume threshold is set at 45 pixels (15 pixels per frame) to remove very small CCs before spreading them to the cloud shield edge in the three-dimensional spatiotemporal space. The volume threshold selected here is determined by the spatial resolution of the H-8/AHI cloud products. The spatial resolution of the cloud products is bound to have a certain impact on the result of the tracking algorithm. For example, using very low-resolution cloud products to execute the tracking algorithm is likely to ignore some relatively small DCSs. However, much better results regarding the DCS evolutions and locations of DCS boundaries will be obtained with high-spatial-resolution products such as H-8/AHI cloud products.

The day of August 7, 2016 was selected to illustrate the technique for identifying and tracking DCSs. Figure 5 shows the DCS segmentation using the TOOCAN-CLP algorithm and the TOOCAN algorithm, as well as the GPM precipitation in the study region. In the TOOCAN algorithm, a threshold of 223 K is employed to detect the convective cores. The iterative process is pushed forward with a 5 K tracking step and is terminated when the cloud shield boundary reaches 253 K. In the example, the TOOCAN algorithm fails to detect the newborn DCSs over the inland region of China in the afternoon (07 UTC) when heavy precipitation occurs around Chongqing Province (marked with a red star) as shown by Fig. 5l. Since the cloud top BTs of the newborn DCSs with low CTH are not particularly cold at the very beginning, they may be higher than the BT threshold. However, due to violent growth, these newborn DCSs often have large optical thickness and can be effectively detected by the TOOCAN-CLP algorithm. Moreover, the CC of the DCS near the Spratly Islands detected by the TOOCAN algorithm (the DCS labelled as A in Fig. 5k) has larger areal extents than the corresponding precipitation location (highlighted by a red rectangle in Fig. 5l), which indicates that ambient anvil clouds of the DCS are mistaken as convective cores by the TOOCAN algorithm. Nevertheless, the CC of the DCS around the East China Sea (the DCS labelled as b, also shown in Fig. 3) detected by the TOOCAN algorithm has less areal extents than the corresponding precipitation location all the time. Contrarily, the distribution of CCs depicted by TOOCAN-CLP algorithm shows high consistency with the pattern of precipitation all over the study region. The atmospheric reanalysis data and surface condition data are used in cloud retrieval to generate AHI cloud top height and cloud optical thickness (Letu et al. 2018), therefore TOOCAN-CLP based on AHI cloud products can get rid of interference from local atmospheric and surface conditions, purely representing cloud properties. It is more universal for different atmospheric environments in different regions. However, both algorithms can handle the splitting and merging events of DCSs. For example, despite the splitting of the large DCS near the west coast of the Philippines (the DCS labelled as c in Fig. 5) in the afternoon, the separated cloud elements are all correctly labelled as the continuation of the previous one without creating new convection artifacts.

Despite the excellent performance in identifying and tracking DCSs, TOOCAN-CLP is based on the VIS and NIR cloud products and thus can only be applied during the daytime. Therefore, in this study, we will present the characteristics of the semi-diurnal variation of DCSs using the TOOCAN-CLP method.

3 Semi-diurnal variation of DCSs

The main aim of this section is to investigate the climatological features of DCSs over Eastern China and its surrounding seas, including their spatial distribution, the semi-diurnal (07:00–17:00 LT) variation of their general properties (size, area, quantity, CTH) and the contrast between land and sea. Several constraints and definitions are applied, the location of the centroid of the DCS is defined by the average longitude and latitude of pixels in the CC and the local time (LT) of the individual DCS is determined by the location of its centroid. DCSs whose centroid is located outside the

red rectangular dashed line marked in Fig. 1 were excluded from the analysis. A DCS is classified as land-type if the centroid of the DCS is located over land surface throughout its lifetime. A similar definition is applied to sea-type DCSs. The single pixel area is obtained by using the Hybeny's distance formula to calculate areas of cloud elements (Sugimoto 1996). DCSs with a CC equivalent radius ($\sqrt{\text{area}/\pi}$) of more than 500 km are categorized as synoptic-scale features and are not discussed in the analysis.

3.1 Semi-diurnal variation of the distribution of DCSs

We divide the DCSs into three classes—small, medium, and large sizes—by using CC equivalent radius boundaries at 25 km and 250 km. The distribution of the initiation of DCSs during the study period is shown in Fig. 6a, c, e, g. Figure 6b, d, f, h exhibit the locations of all three classes of DCSs. As can be seen from Fig. 6a, almost no DCSs initiate over land except inland China in the morning. However, convection experiences exuberant initiation over all land regions in the afternoon as the land surface or overlying atmospheric boundary layer warms up (Fig. 6e, g). In the late afternoon, small and medium-sized DCSs are distributed more densely over the coastal land region (e.g., the coastal region of China and Western Luzon) than over the inland regions (Fig. 6h). Over the sea, convective systems also initiate vigorously in the afternoon when the sea surface temperature reaches its diurnal peak, especially over tropical sea areas (Fig. 6g). Small and medium-sized sea-type DCSs are distributed all over the sea but are more exiguous over the east coast of the Indochinese Peninsula and sub-tropical sea areas.

Over continental Eastern China, large DCSs are first identified over the eastern periphery of the Tibetan Plateau and central Eastern China in the morning (Fig. 6b) then over the southeastern coastal region in the afternoon (Fig. 6h). It seems that the occurrence of large DCSs over Eastern China shows an eastward diurnal phase delay. The eastward diurnal phase delay of a long-duration rainfall event is a prominent feature along the Yangtze River in summer (Chen et al. 2010). Furthermore, the number of large DCSs over the inland region of China is reduced significantly from the morning to the afternoon. Over the sea, large DCSs are more densely distributed over the northern South China Sea and the coastal seas of the Philippines, Korea, and Japan. In contrast, there are almost no large DCSs over the East China Sea and the coastal sea east of the Indochinese Peninsula. Moreover, the distribution of large DCSs over the coastal sea west of the Philippines is greater than the east of the Philippines. The same phenomenon is also seen over Taiwan. It can be inferred that large organized DCSs tend to occur over the coastal sea areas, especially the windward side in the southwest monsoon region during summer.

3.2 Semi-diurnal variation of DCS properties

The semi-diurnal variation of DCSs detected over the study domain are shown in Fig. 7. The number of small DCSs over land continues to reduce from 07:00 LT to 10:00 LT, accompanied by a notable decrease in the area of CC and SR, which indicates that most of these DCSs are in their dissipation stage (Fig. 7a, d). Then the number of small continental DCSs increases dramatically around 10:00 LT, with an evident peak in the afternoon around 16:00 LT (Fig. 7a). Over the sea, there is also an increase in the number of small DCSs after 10:00 LT, with a simultaneous increase in CC and SR coverage (Fig. 7a, d). It can be concluded that the occurrence of small DCSs, especially those over land, is related to the local thermal heating regulated by solar radiation. For medium-sized DCSs over land, the occurrence of DCSs increases sharply around 12:00 LT, two hours behind that of the small continental DCSs (Fig. 7a, b). Since CC and SR coverage increases rapidly during the development stage of DCSs, it can be inferred that most medium-sized continental DCSs develop from small ones whose CTH is gradually increasing. However, medium-sized DCSs over the sea exhibit a weak diurnal cycle with an almost constant occurrence from 07:00 LT to 17:00 LT and slight increase of CTH (Fig. 7b, h).

The diurnal amplitude of the number of large DCSs over land is much smaller than that of small and medium-sized DCSs (Fig. 7c). This suggests that these large DCSs are less sensitive to the diurnal cycle of the surface thermal effect. Similarly, the number of large sea-type DCSs also shows no clear semi-diurnal variation. Besides, large DCSs over the sea may undergo gradual dissipation, indicated by the persistent decrease in the CTH of the CC and SR throughout the daytime (Fig. 7i). Furthermore, for all three classes, the ratio of the areas of the SR and CC of DCSs over the sea is always larger than that of DCSs over land. This is probably because the atmospheric moisture condition over the sea is more favorable for sediment ice detrained from the CC to transform into SR by deposition, which releases latent heat and eventually forms mesoscale updrafts that can maintain the SR for a long time (Feng et al. 2012).

Finally, the semi-diurnal variation of DCS number over the tropical and sub-tropical regions is investigated respectively (Fig. 7j–l). The continental DCSs over the tropical region show similar semi-diurnal cycles of occurrence to those over the sub-tropical region. Over the sea, tropical DCSs make up a large majority of sea-type DCSs in the study region. It is noteworthy that the semi-diurnal cycle of DCSs over the tropical sea areas is more significant than that over the sub-tropical sea areas, especially for small and medium-sized classes. Thus the semi-diurnal variation of sea-type DCSs in the study region is mainly attributed to the variation of DCSs over the tropical sea areas.

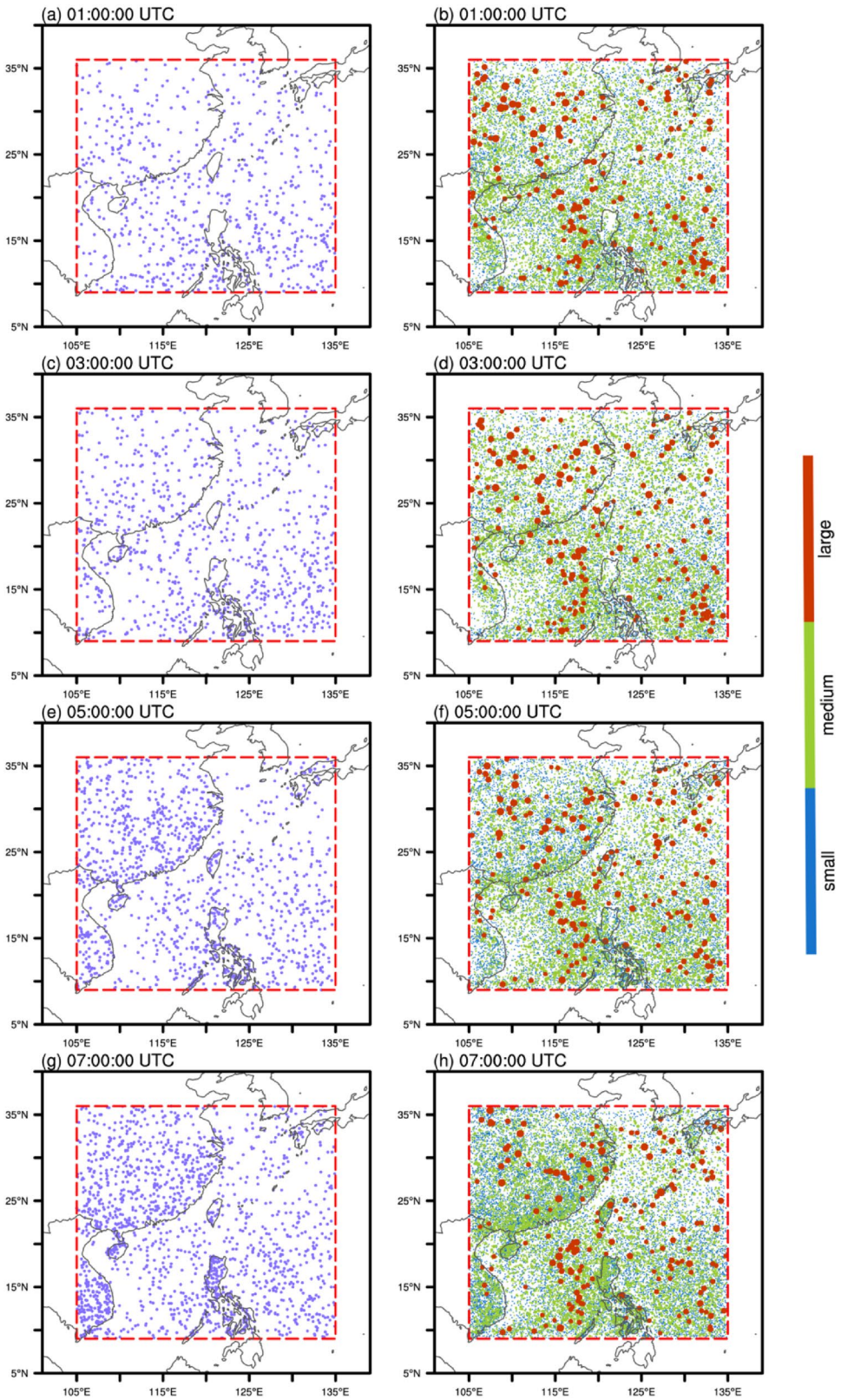

Fig. 6 Distribution of the initiation of DCSs (**a**, **c**, **e**, **g**), and the locations of all existing DCSs for three size classes defined by the CC equivalent radius boundaries at 25 km and 250 km (**b**, **d**, **f**, **h**) during the study period. The size of the solid circle is proportional to the actual CC size of the convection

To further examine the semi-diurnal features of DCSs of different sizes, the mean cloud coverage at different CTHs for three size classes throughout the daytime is shown in Fig. 8. For small-sized DCSs over land, the mean area covered by cloud tops greater than 10 km reaches its maximum at about 16:00 LT, which is about two hours behind the time

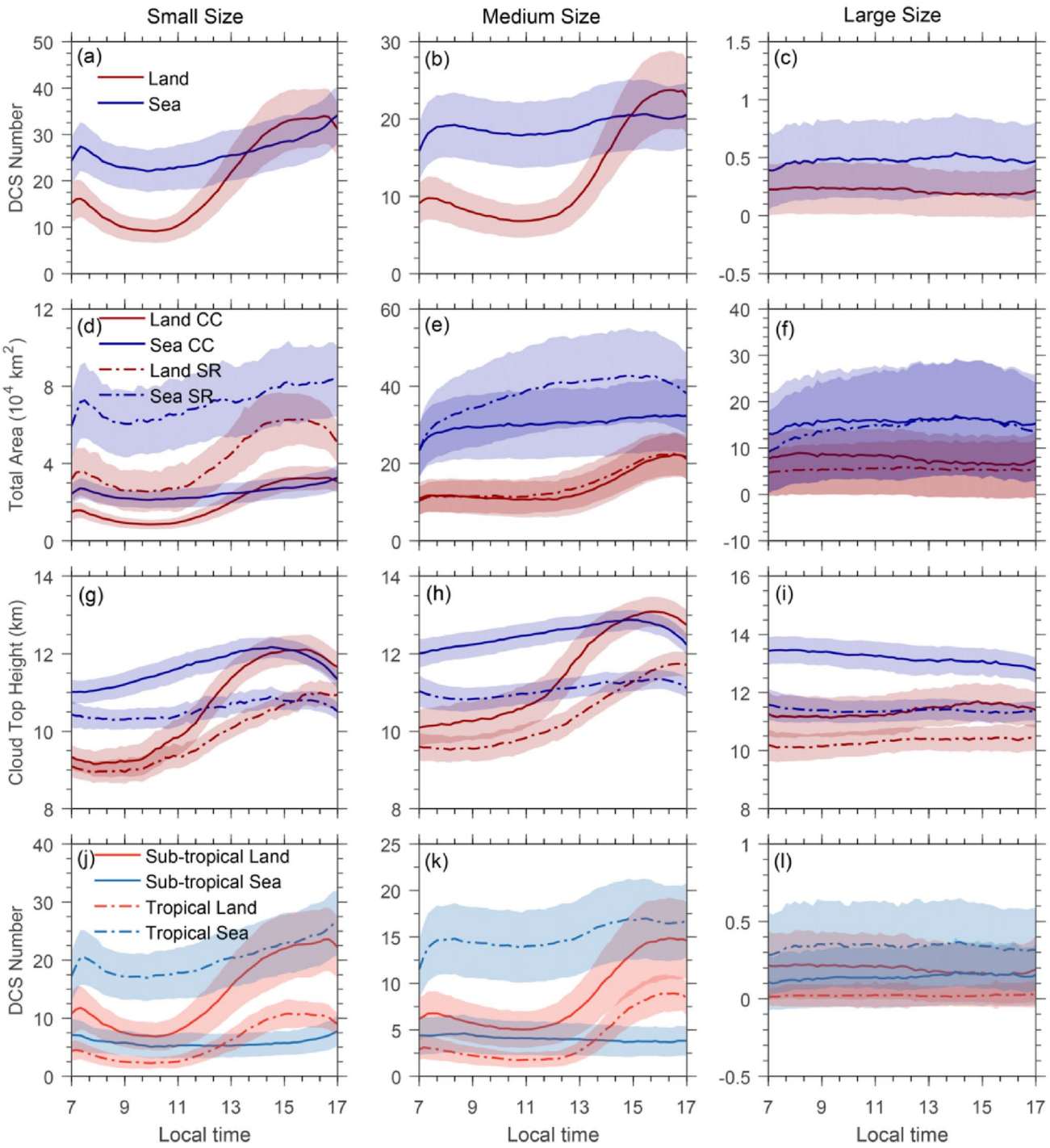

Fig. 7 Semi-diurnal variation of properties of DCSs over land (red lines) and sea (blue lines) in terms of DCS number (**a**–**c**), CC (solid line) and SR (dot-dashed line) total areas (**d**–**f**), and CC and SR cloud top height (**g**–**i**) for the three size classes (small, first column; medium-size, second column; large, third column) defined by CC equivalent radius boundaries at 25 km and 250 km. The fourth row also shows the semi-diurnal variation of DCS number over the tropical and sub-tropical regions respectively (**j**–**l**). The shaded areas show the standard errors

when the land surface reaches its warmest temperature by solar heating (14:00 LT). This indicates that the environment still favors the development of DCSs from 14:00 LT to 16:00 LT. After 16:00 LT, the mean area covered by cloud tops greater than 10 km starts to decrease. The maximum afternoon coverage of high CTH implies strong dependence

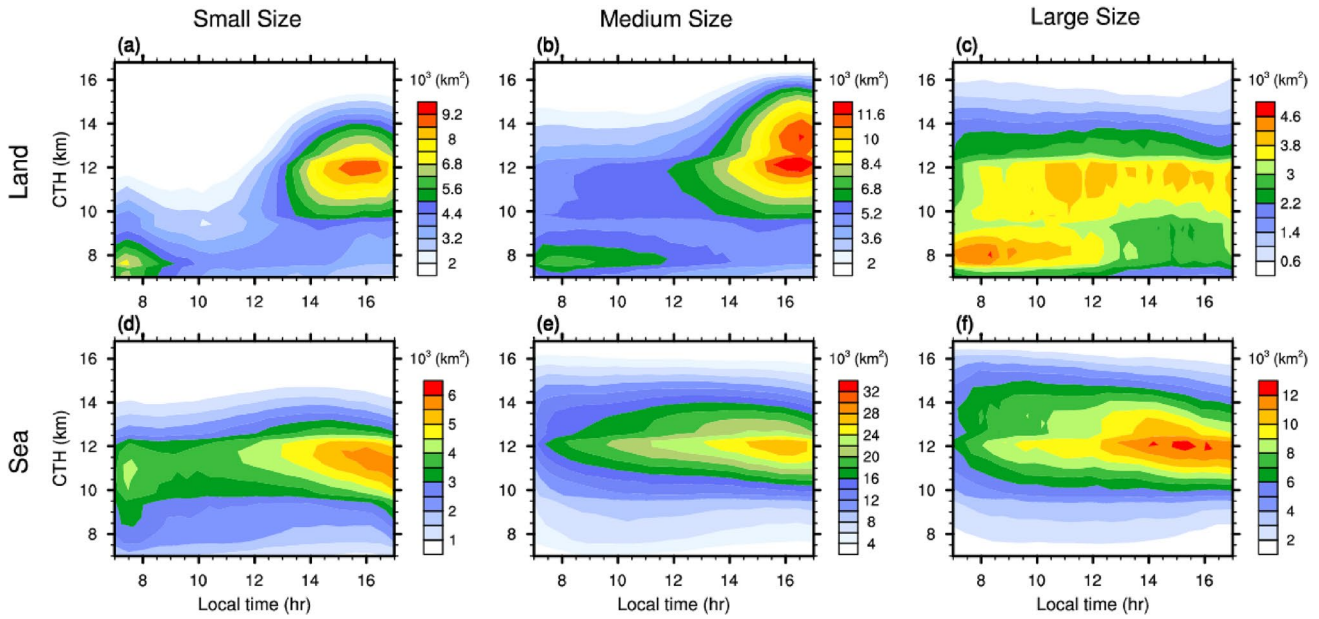

Fig. 8 Semi-diurnal variation of the mean cloud coverage for particular CTHs (within each 0.2 km interval) in CC and SR regions for three size classes of DCSs (small, first column; medium-sized, second column; large, third column) as defined by the CC equivalent radius boundaries at 25 km and 250 km over land (top row) and sea (bottom row). The color bar represents the mean cloud coverage ($\times 10^3$ km^2)

of small-sized DCSs on local thermal instability. Over the sea, most small convective systems develop vigorously in the afternoon as well since the peak of the mean area covered by cloud tops greater than 12 km is found at 14:00–15:00 LT when the sea surface temperature reaches its diurnal peak. For medium-sized DCSs over land, the mean area covered by CTH between 10 and 16 km increases sharply from 12:00 LT, two hours behind small ones, peaking at about 16:00 LT. However, medium-sized sea-type DCSs, which comprise the majority of the total cloud coverage over the sea, exhibit a slight increase in coverage for CTH between 14 and 16 km, which is much less significant than medium-sized DCSs over land. This may explain the weaker diurnal cycle of DCSs over the sea compared to that over land. The formation of DCSs over the sea could happen at any time of day and is always linked to convective activity such as cold pools (Chen and Houze 1997a).

For large DCSs over land, there is a decrease in coverage for CTH greater than 14 km from 07:00 LT to 15:00 LT and only a slight increase for extremely high CTH after 15:00 LT, which suggests that most of these large cloud systems are in their late mature and dissipation periods before 15:00 LT. The occurrence of large DCSs over the coastal region of China in the afternoon (Fig. 6h) may account for the slight increase in the extremely high CTH after 15:00 LT. Over the sea, the mean coverage of high cloud tops (> 14 km) in large DCSs decreases throughout the daytime, indicating the weakening of these DCSs in their life cycle. Whereas, clouds with a top height between 10 and 14 km in the large sea-type DCSs reach the maximum mean coverage in the late afternoon. The anvil clouds associated with convective cores in DCSs are mostly produced by the maturing or decaying of intense, vertically extending convective cells (Houze Jr 2004). Therefore, relatively warm clouds (10–14 km) may be partly transformed from colder clouds (14–16 km) with a gradual decrease of coverage. On the whole, the semi-diurnal cycle of DCSs is more complicated than we expected considering different cloud systems have different areal extents and lifetimes.

3.3 Semi-diurnal variation of precipitation relevant to DCSs

This section examines the daily mean distribution of GPM satellite precipitation (Fig. 9a) in the region of study prior to investigating its diurnal cycle. Over continental Eastern China, there are notable precipitation maxima over Southern China as well as the middle and lower valleys of the Yangtze River. Interestingly, rainfall over the coastal sea is inclined to occur on the windward side of the continent (e.g., coastal sea west of the Philippines) as southwest monsoons dominate the surrounding seas of Eastern China. Next, the harmonic analysis approach is employed to analyze the diurnal cycle of precipitation in the region of study (Dai and Deser 1999; Love et al. 2011; Roy and Balling Jr 2005). Figure 9b shows the map of the local time for the maximum of the first

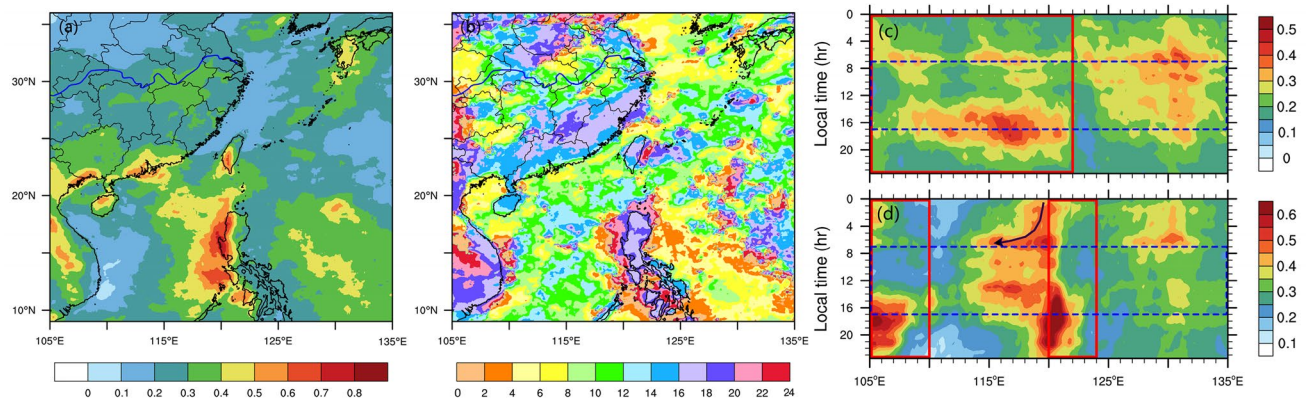

Fig. 9 Daily mean precipitation (mm h^{-1}) obtained from GPM satellite precipitation products (**a**). Phase of the first harmonic of precipitation in terms of the local time of the maximum (**b**), and the blue line indicates the Yangtze River. Time-longitude plot of precipitation, averaged from 23.5° N to 36° N (**c**) and from 9° N to 23.5° N (**d**). Black line with an arrow indicates the migrating directions of the offshore nocturnal rainfall over the coastal sea west of the Philippines. The areas within the red lines are continental regions and those outside are sea regions. The period within the blue dashed lines is from 07:00 LT to 17:00 LT

harmonic of precipitation. The peak in precipitation tends to occur in the late afternoon and evening over most of the continental region except the Yangtze River Valley and the region west of 110° E over Eastern China. Over the coastal sea, maximum precipitation tends to occur in the early morning near the coast but several hours later some distance away from the coast (e.g., coast of Southern China). In particular, the diurnal cycle of precipitation off the west coast of the Philippines has an extremely obvious mode of offshore-directed propagation towards the adjacent sea.

To further investigate the diurnal variation of precipitation, the time-longitude plot of precipitation is depicted in Fig. 9c, d. As also shown in Fig. 9c, d, all the three continental regions (i.e., Eastern China, Philippines, and Eastern Indochina Peninsula) exhibit similar features, that is, maximum rainfall occurs in the late afternoon or evening. Besides, the Eastern China region also has an obvious rainfall peak in the early morning. The occurrence of a rainfall maximum in the region west of 110° E over Eastern China at midnight or in the early morning has been identified in previous research (Chen et al. 2010; Yu et al. 2007). Such a feature has also been observed in the middle and lower valleys of the Yangtze River and over the South China coastal region (Bao et al. 2011; Huang and Chan 2011; Jiang et al. 2017).

For the sea areas, an early morning rainfall peak over the South China Sea was found at around 06:00 LT (Fig. 9d). Ho et al. (2008) and Park et al. (2010) showed that a morning rainfall peak off the coast of the Philippines is a prominent characteristic during the Asian summer monsoon. The cloud system contributing to the early morning precipitation maximum over the South China Sea is considered to be initiated over the coastal sea west of the Philippines before dawn, which produces heavy rainfall in the morning and gradually dissipates until the afternoon (Park et al. 2010). Moreover, the nocturnal offshore rainfall, which is generated off the South China coastline and subsequently moves to the open sea from night to morning, may also be associated with the morning rainfall peak (Chen et al. 2016). In addition to the early morning precipitation peak, it is interesting that the diurnal cycle of rainfall over the South China Sea shows another rainfall maximum in the early afternoon (Fig. 9d). The existence of twin peaks in the diurnal precipitation cycle is consistent with the results of Li et al. (2010), which shows that the diurnal cycle over the northern part of the South China Sea has two rainfall peaks—one in the early morning, the other in the afternoon—following the onset of the summer monsoon. The twin peaks in rainfall over the South China Sea could be closely related to the latent heat flux, which has two maximums at 03:00–06:00 LT and 13:00–15:00 LT after the onset of the monsoon (Yan et al. 2007). The latent heat flux is strongly associated with the quantity of water vapor and the local thermal instability, which is directly associated with the DCS precipitation. Besides, the intensity of rainfall over the East China Sea and Philippine Sea reaches its peak around 06:00–08:00 LT (Fig. 9c, d). Ramage (1952) analyzed the diurnal variation of rainfall during the summer from May to August over the coastal regions of Japan, Korea and Eastern China, where the monsoon prevailed, and found that all these regions had a morning precipitation maximum. In summary, the study region has a prominent peak in precipitation in the late afternoon or evening over land and an early morning peak over the sea. In addition, there is an early morning peak in rainfall over Eastern China and an early afternoon peak over the South China Sea.

To explore how the DCSs contribute to the diurnal cycle of precipitation during the daytime, Fig. 10 shows the

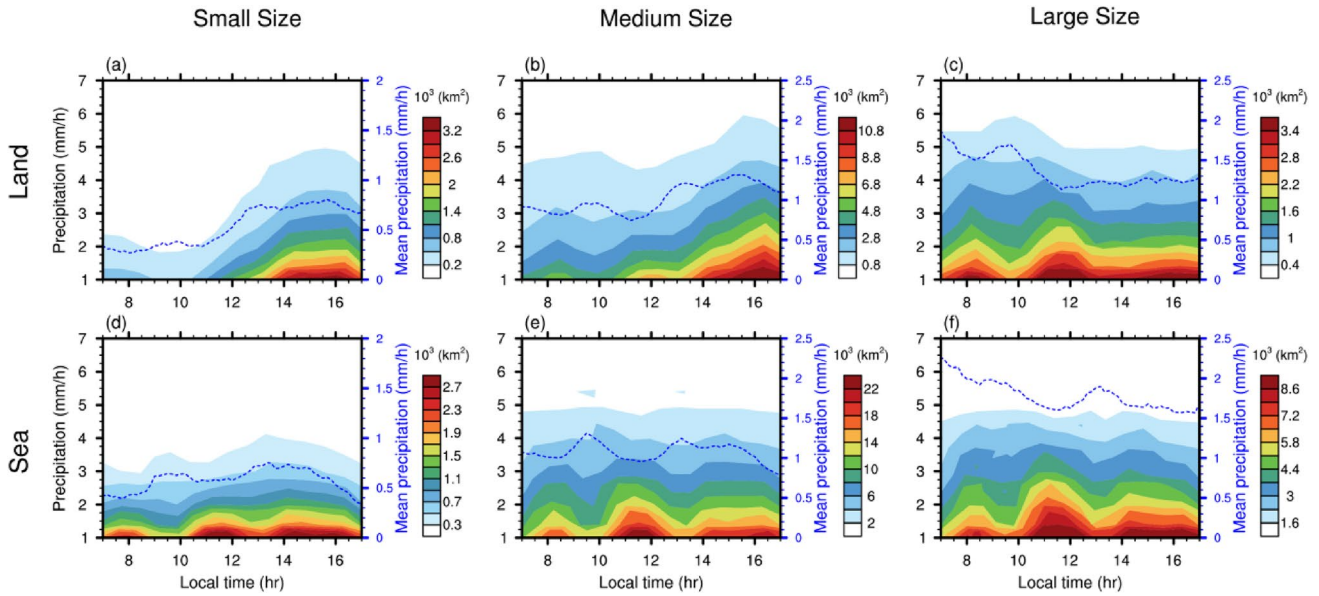

Fig. 10 Semi-diurnal variation of mean coverage at particular precipitation intensities (within each 0.2 mm h^{-1} interval, shaded) and mean precipitation (mm h^{-1}, blue dashed line) in CC and SR regions for three size classes of DCSs (small, first column; medium-sized, second column; large, third column) defined by CC equivalent radius boundaries at 25 km and 250 km over land (top row) and sea (bottom row). The color bar represents the mean coverage ($\times 10^3$ km^2)

semi-diurnal variation of the mean coverage at different precipitation intensities and the mean precipitation for three size classes of DCSs. It is seen that the mean precipitation intensity of large convection is always larger than that of small and medium-sized convection, both over land and sea. For small continental DCSs, the highest precipitation occurs at about 16:00 LT when the CTH of DCSs also reaches its maximum (Figs. 7g, 10a), while the maximum precipitation of small sea-type DCSs occurs in the early afternoon (Fig. 10d) around 14:00, a bit earlier than that of the continental DCSs. For medium-sized continental DCSs, the mean coverage of precipitation at any intensity increases sharply from 12:00 LT, two hours behind the increase for small continental ones, similar to the feature of CTH. The intensity and coverage of the rainfall of medium-sized DCSs over the sea, however, exhibit no significant semi-diurnal cycle.

As shown in Fig. 10c, large continental cloud systems mainly experience a gradual decrease in average precipitation intensity and mean area covered by precipitation between 3 and 5 mm h^{-1} during the daytime. At the same time, the mean precipitation intensity of large sea-type DCSs also shows an observable decline (Fig. 10f). It can be inferred that most large DCSs, especially those over the sea, may undergo gradual dissipation during the daytime, as also shown by their semi-diurnal cycle of CTH. In summary, the semi-diurnal variation of precipitation shows almost the same pattern as that of CTH for DCSs of identical sizes and surface types. Moreover, the complex semi-diurnal cycle of precipitation over the study domain is not related only to a certain type of DCSs but derived from the combination of the semi-diurnal cycles of different types of DCSs.

4 Mechanisms related to the semi-diurnal variation of DCSs

In this section, we examine the mechanisms behind the semi-diurnal cycle of DCSs over Eastern China and its surrounding seas. Every summer, the southwest monsoon dominates the Indian Ocean, the South China Sea, and far-western North Pacific, which promotes the transport of moisture from the equatorial oceans into the subtropical continents, resulting in an increase of the convective instability over a large area. The sea–land breeze is a local circulation caused by the thermal contrast between sea and land. Under the assumption that large-scale wind has relatively weak temporal variation, the local sea–land breeze (wind anomalies) can be acquired by subtracting the daily mean winds from the total winds (Chen et al. 2016; Huang et al. 2015; Shen et al. 2019). Although this assumption may bring some uncertainties (Krishnamurti and Kishtawal 2000), this convenient estimate of sea–land breeze circulation could offer us worthwhile information. Next, the diurnal variation of meteorological fields based on JRA-55 reanalysis is examined and displayed in Figs. 11, 12, 13 and 14.

In the afternoon (06:00 UTC; 14:00 LT), large positive temperature anomalies occur over the continent and adjacent sea. However, the thermal properties of the sea surface

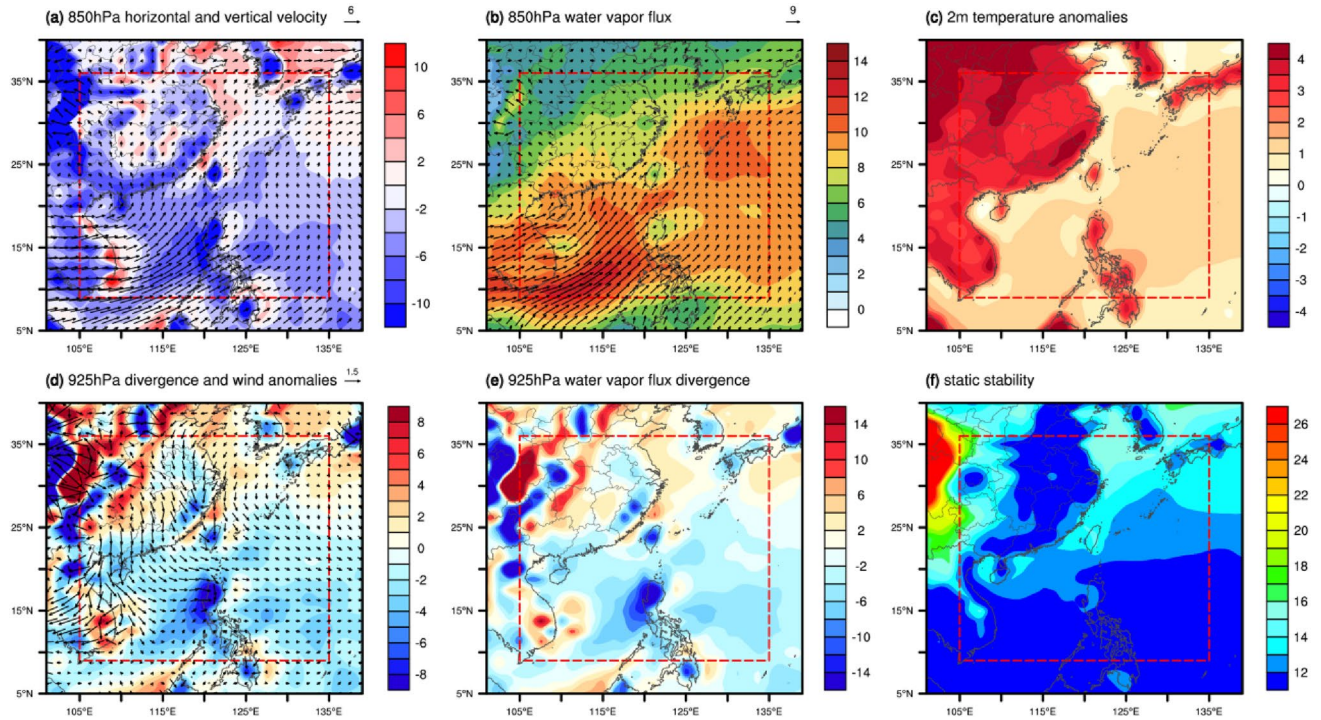

Fig. 11 Composite zonal and meridional wind velocity (vectors; m s^{-1}) and vertical velocity (shaded; 10^{-2} Pa s^{-1}) at 850 hPa (**a**), water vapor flux (vector and shaded; g/(s hPa cm)) at 850 hPa (**b**), 2 m temperature anomalies (UTC-daily mean; shaded; K) (**c**), divergence (shaded; 10^{-6} s^{-1}) and wind anomalies (vectors; m s^{-1}) at 925 hPa (**d**), water vapor flux divergence (shaded, 10^{-8} g/(s hPa cm^2)) at 925 hPa (**e**) and static stability ($\theta_{700hPa} - \theta_{2\text{-}m}$; shaded; K) (**f**) at 06:00 UTC obtained from JRA-55 atmospheric reanalysis data for summertime from 2016 to 2018 over the study domain

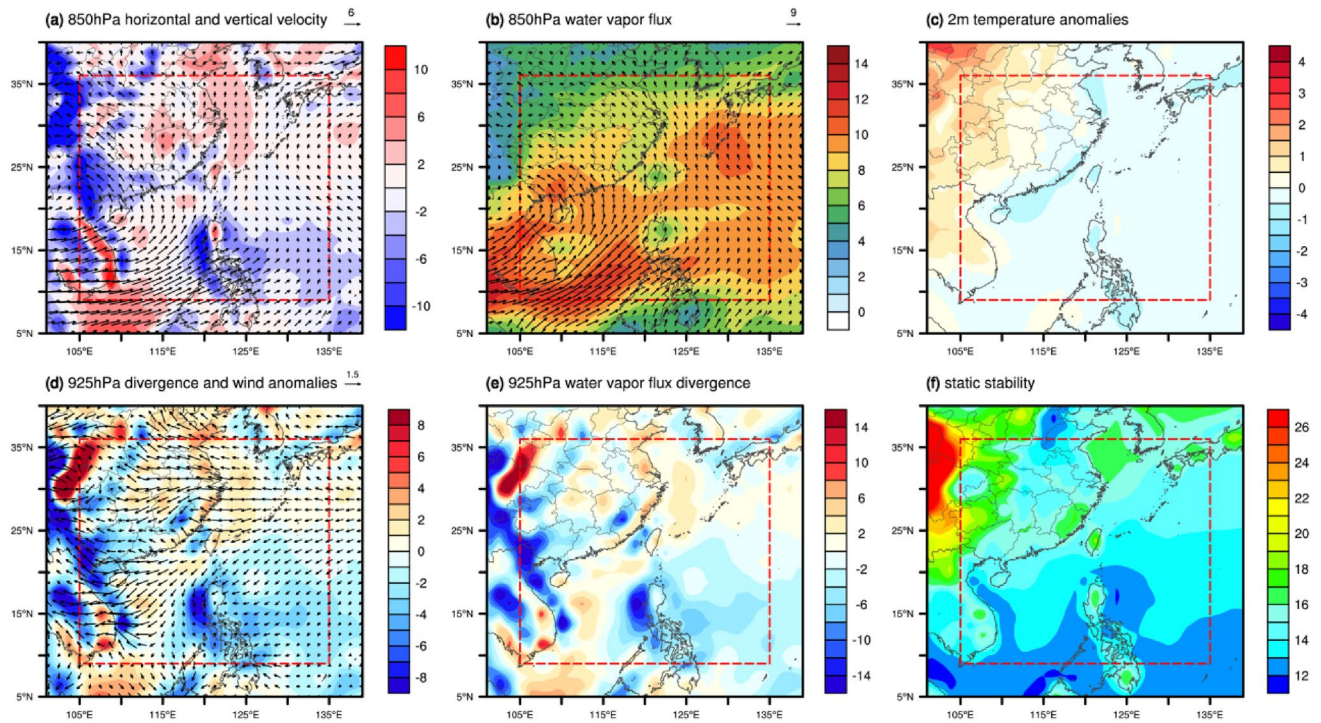

Fig. 12 As in Fig. 11 but for 12:00 UTC

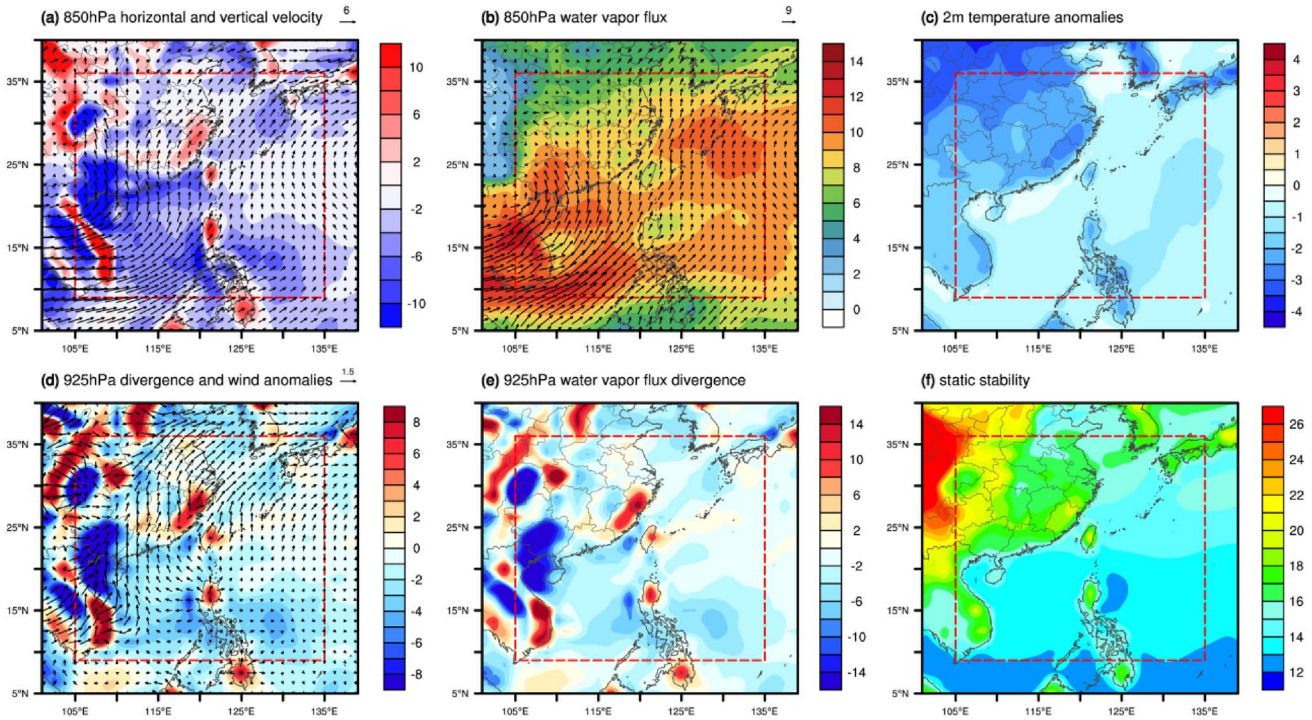

Fig. 13 As in Fig. 11 but for 18:00 UTC

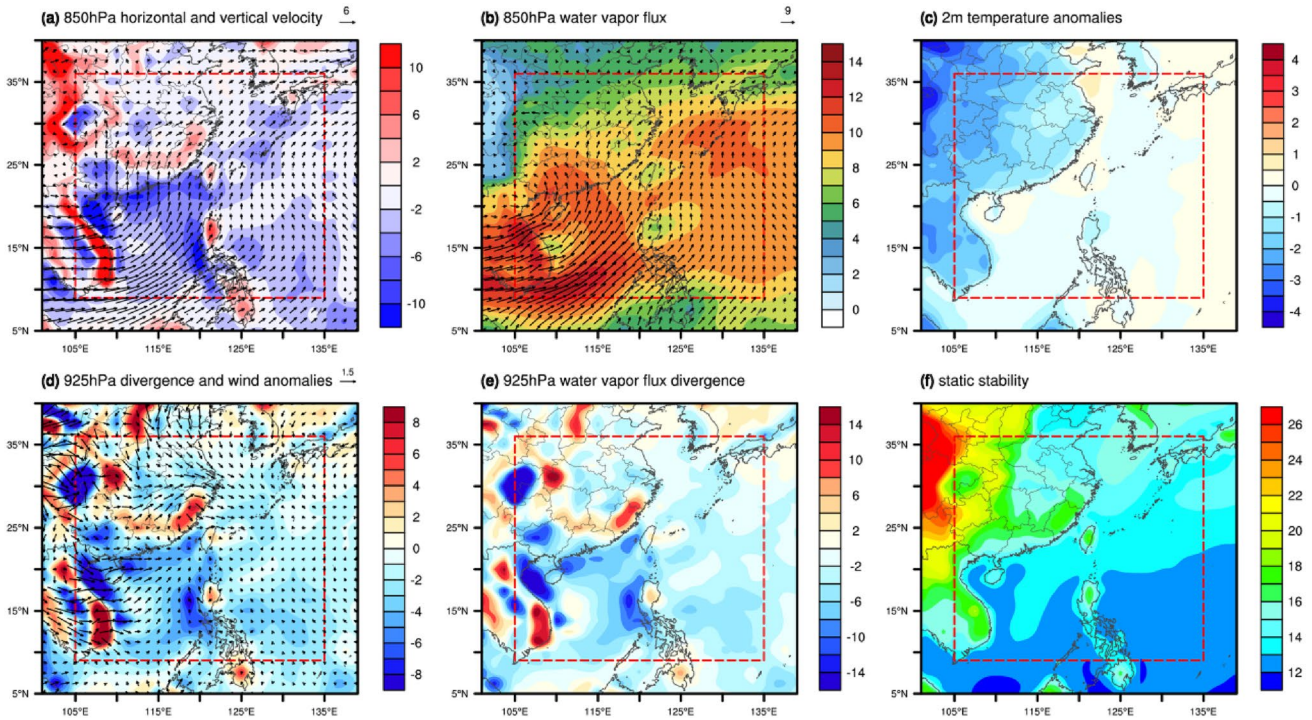

Fig. 14 As in Fig. 11 but for 00:00 UTC

undergo a diurnal cycle that is relatively weak compared with that of the land surface (Fig. 11c). The solar radiation on the underlying surface and the overlying atmospheric boundary layer leads to local thermal instability (Fig. 11f)

and provides a favorable environment for the initiation and growth of convective systems over both land and sea (especially tropical sea areas) (Chen and Houze 1997a). As a result, the number of small and medium-sized DCSs over land exhibit a maximum in the afternoon (Fig. 7a, b). The occurrence of small sea-type DCSs, especially those over the tropical region, varies analogously to that of the small continental DCSs but with smaller amplitude (Fig. 7j). In addition, small and medium-sized DCSs are distributed more densely over the coastal region of southeastern China and western Luzon than over the inland regions (Fig. 6h). Many studies have proposed that, in addition to the solar heating effect, sea breeze circulation is also associated with the convective afternoon rainfall along the coast during the daytime (Chen et al. 2016; Huang et al. 2016; Simpson et al. 2007). Moreover, the existence of a coastal mountain range leads to stronger precipitation over the windward side by deepening the sea breeze (Riley Dellaripa et al. 2020). As shown in Fig. 11d, the westerly component of low-level wind is significantly accelerated by the sea breeze. The impingement of the sea breeze on the high mountains over western Luzon induces strong local convergence and upward motion (Fig. 11a, d), generating convection of heavy rainfall along the coast in the afternoon (Fig. 6g).

After sunset (12:00 UTC; 20:00 LT), negative temperature anomalies and downward motion dominate vast regions (Fig. 12a, c), which inhibit the further growth of the afternoon convective storms. As pointed out by Rickenbach and Rutledge (1998), sub-mesoscale clouds, which are typical of land-based convection and extend only to the mid-troposphere, enter into their mature or declining stage during the afternoon and evening. It can be seen from Fig. 7g and h that the CTHs of small and medium-sized continental DCSs begin to decline in the late afternoon. In general, the occurrence of small and medium-sized continental DCSs exhibits a maximum in the afternoon, and this remarkable semi-diurnal variation is mainly dominated by solar thermal heating and local sea breeze circulation. The diurnal heating of the tropical sea surface can also favor the vigorous formation of DCSs (especially the small ones) in the afternoon but these DCSs undergo a diurnal variation that is relatively weak compared with continental DCSs.

At night (18:00 UTC; 02:00 LT), the thermal contrast between land (e.g., the Philippines, Taiwan) and sea, and the cold pool induced by convection over land in the afternoon, strengthens the offshore breeze. The interaction between the large-scale southwesterly winds and offshore breeze gives rise to the low-level offshore convergence, which help trigger the convective updrafts. The strong ascending motion off the west coast of the Philippines and Taiwan (Fig. 13d) indicates the initiation and growth of DCSs. As shown in Fig. 6, large organized DCSs tend to occur over the windward coastal sea of the continent, such as the coastal sea west of the Philippines and Taiwan. The role of the large-scale prevailing onshore wind as well as its interaction with the local circulation in generating convective systems accompanied by nocturnal offshore rainfall has been confirmed by numerous previous studies (Chen et al. 2019b; Xie et al. 2006; Yu and Jou 2005). Over continental Eastern China, the prevailing southwesterly or southerly winds help transport warm and moist air from lower latitudes, leading to a strong water vapor flux over Eastern China (Fig. 13b). In the region west of 110° E, strong upward motion and convergence (Fig. 13a, d) as well as water vapor flux convergence (Fig. 13e) provide preferable conditions for the formation of organized convection over the eastern periphery of the Tibetan Plateau and Southern China at midnight.

In the morning (00:00 UTC; 08:00 LT), the local offshore flow weakens due to the decreasing temperature contrast between the land and sea surface. But meanwhile, the large-scale southwesterly winds over the South China Sea accelerate, and strong ascending motion and low-level convergence cover the sea off the west coast of the Philippines and the northern South China Sea (Fig. 14a, d). Therefore, the environment is still favorable for the development and subsistence of DCSs at this time. Over continental Eastern China, low-level southwesterly winds still prevail. Due to the deceleration of winds north of the Yangtze River, low-level convergence dominates the middle and lower valleys of the Yangtze River at this time (Fig. 14d), promoting the development of convection, especially those of large sizes and long durations. As can be seen from Fig. 6b, in the morning, large continental DCSs are distributed all over inland China from the eastern periphery of the Tibetan Plateau to the middle and lower valleys of the Yangtze River.

However, after sunrise, solar radiation at the cloud top increases the stability and therefore depresses the convections. In the meantime, the land breeze weakens, and the offshore convergence disappears, thus the nocturnal clusters over the sea start to dissipate with a gradual decrease in CTH and precipitation during the daytime (Figs. 7i, 10f). Over inland China, the strength of the southwesterly winds reduces with the weakening of water vapor flux and convergence after 08:00 LT. Consequently, nocturnal convections over the inland region gradually decay accompanied with the reduction of strong precipitation cover during the daytime (Fig. 10c). Given the above, unlike small and medium-sized DCSs, large convective storms are less dominated by solar thermal heating or local circulation and show a weaker semi-diurnal cycle. Large DCSs over the inland region mainly initiate from the large-scale prevailing southerly or southwesterly winds over Eastern China at night. The generation of large DCSs over the windward coastal sea of the continent is closely associated with the interaction between the local offshore breeze and onshore large-scale monsoon flows. Most

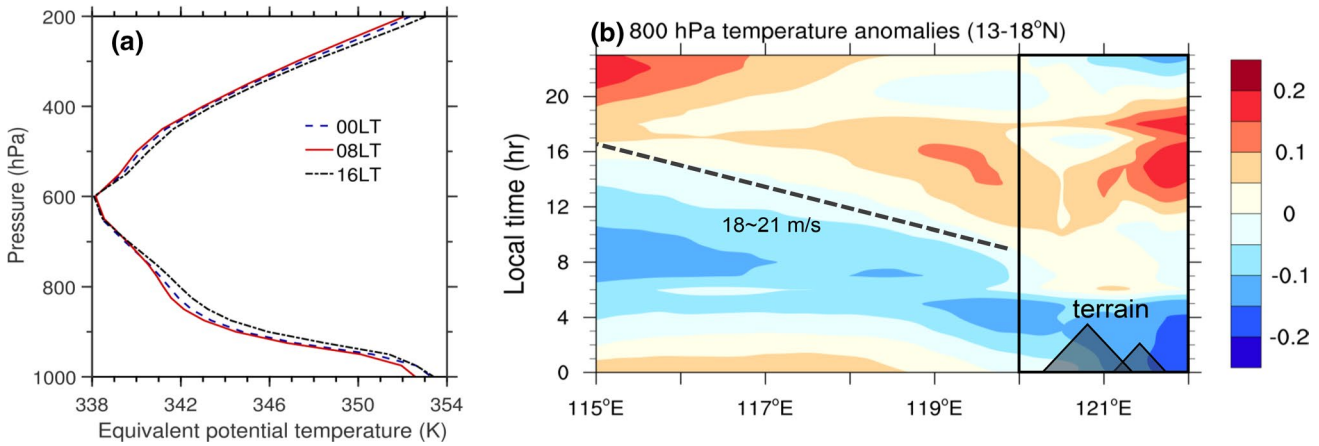

Fig. 15 Mean profiles of equivalent potential temperature averaged over the coastal sea west of Luzon (115° E–119° E, 13° N–18° N) (**a**), and mean diurnal variation of temperature anomalies averaged over 13° N–18° N, obtained from hourly ERA5 atmospheric reanalysis data for summertime from 2016 to 2018 (**b**)

of these large DCSs gradually dissipate during the daytime as the environment becomes less favorable.

Apart from the interaction between large-scale atmospheric circulation and local offshore breeze, another mechanism involving gravity waves has also been proposed to contribute to the offshore DCSs (Hassim et al. 2016; Mapes et al. 2003; Mori et al. 2004). The coastal sea west of Luzon is chosen to examine the gravity wave mechanism due to its obvious offshore propagation of the diurnal phase of precipitation (Fig. 9b). Figure 15a shows the mean profiles of equivalent potential temperature averaged over the coastal sea west of Luzon. The figure shows that profiles at different times possess similar features but 08:00 LT is much more destabilized, especially below 800 hPa as shown by its larger depression of equivalent potential temperature. The time evolution of 800 hPa temperature anomalies associated with the passage of the gravity waves is shown in Fig. 15b as a time-longitude plot. The propagation of the gravity wave signal is evident in Fig. 15b, with a phase speed of approximately 18–21 m s^{-1}. The cool phase of the gravity waves (negative temperature anomalies center) propagates offshore from midnight to early morning, destabilizing the offshore environment, which certainly provides beneficial conditions for the development and maintenance of offshore DCSs. Moreover, the migration of these DCSs towards the offshore region is probably through the gravity wave since the migration speed of offshore rainfall is close to the gravity wave speed (Figs. 9d, 15b). Therefore, both the gravity wave mechanism and the interaction between large-scale prevailing onshore wind and local circulation are thought to be related to the large offshore DCSs, especially those accompanied by strong precipitation and located over the windward coastal sea of the continent.

5 Conclusions

To study the semi-diurnal variation of DCSs over Eastern China and its surrounding seas in summer, the TOOCAN algorithm was modified by employing the H-8/AHI cloud property products instead of original brightness temperature and was renamed as TOOCAN-CLP. In TOOCAN-CLP, DCSs are first identified based on the CTH and COT obtained from cloud property products, and then tracked in a three-dimensional spatiotemporal space starting from the CC and progressing to the associated anvil cloud edges through an iterative process. Compared to the algorithm based on single-band BT, the modified algorithm can get rid of interference from local atmospheric and surface conditions and purely represent cloud properties. It is therefore more universal for different atmospheric environments over a wide region. Additionally, the modified algorithm has an improved ability to identify convective cores that have similar brightness temperatures as the connected anvil cloud but are thicker and have stronger precipitation. Moreover, the new algorithm is capable of detecting DCSs at early developmental stages when their brightness temperature is not particularly cold but cloud thickness is sufficiently high. In summary, the new algorithm performs excellently in identifying and tracking DCSs.

To investigate the typical features of the semi-diurnal cycle of DCSs with different horizontal sizes and over different surface types, we classify the detected DCSs over land and sea into small, medium, and large sizes based on the convective core (CC) equivalent radius. The small and medium-sized DCSs over land exhibit a maximum occurrence in the afternoon, which is mainly due to local thermal instability. Furthermore, these convective storms are more

prevalent over coastal regions as a result of sea breeze circulation along the coast. Solar heating on the sea surface can also provide a favorable environment for the formation of DCSs, leading to an abrupt increase in the number of small DCSs over the tropical sea areas during the daytime, which is similar to that of continental DCSs but with a smaller amplitude of variation. Medium-sized DCSs, which account for the majority of the total coverage over the sea, exhibit a weak diurnal cycle in terms of occurrence and precipitation.

Unlike small and medium-sized DCSs, large convective storms are less dominated by solar thermal heating and local circulation. The occurrence of large DCSs over both land and sea shows a weak diurnal variation. Large DCSs over inland China mainly initiate from the large-scale prevailing southerly or southwesterly winds at night. As the water vapor flux by southwesterly winds gradually weakens in the daytime, these large DCSs gradually enter into their mature and dissipation stages, with a decrease in the area covered by high CTH and strong precipitation. The large offshore DCSs accompanied by heavy rainfall always form over the windward coastal sea of the continent. These DCSs are closely associated with the interaction between the local offshore breeze and onshore large-scale southwesterly winds, as well as the gravity waves. As the land breeze weakens after sunrise, offshore convergence disappears. Consequently, these nocturnal DCSs over the sea dissipate with a gradual decrease of CTH and precipitation intensity during the daytime.

The TOOCAN-CLP algorithm employing cloud property products to detect and track DCSs paves the way for the better characterization of DCS morphological and physical properties at a high spatiotemporal resolution. This algorithm can also be used to explore more detailed features of DCSs and their related mechanisms and dynamics, which would help to improve the simulation of cloud processes in numerical models. Despite the excellent performance of the TOOCAN-CLP algorithm in identifying and tracking DCSs, the VIS and NIR cloud products can only be available during the daytime, so the current algorithm is limited to the daytime execution. The rapid retrieval algorithm of cloud products based on thermal infrared channels (lacking official products now) is urgent to be developed. Thus, the current TOOCAN-CLP algorithm can be executed by using thermal infrared cloud properties and applied to examine DCSs from a more comprehensive perspective (e.g., full life cycle of DCS, duration of DCS) in future work.

Acknowledgements The work was supported by the National Key R&D Program of China (2019YFC1510103), the National Natural Science Foundation of China (41675003, 41705039). We thank the anonymous reviewers for their constructive comments and Professor Zhaohua Wu for his editorial efforts. We also thank Dr. Fuchang Wang for his help in revising the manuscript. We gratefully acknowledge the P-Tree System, Japan Aerospace Exploration Agency (JAXA) for providing Himawari-8/Advanced Himawari Imager (H-8/AHI) level-2 operational cloud products. The Integrated Multi-satellitE Retrievals for GPM (IMERG) data were provided by the NASA/Goddard Space Flight Center and Precipitation Processing System (PPS), which develop and compute IMERG as a contribution to GPM constellation satellites, and were archived at the NASA Goddard Earth Science Data and Information System Center (GES DISC). We also acknowledge the Japanese 55-year Reanalysis (JRA-55) conducted by the Japan Meteorological Agency (JMA), and the fifth generation ECMWF (European Centre for Medium-Range Weather Forecasts) atmospheric reanalysis (ERA5) produced by ECMWF.

References

Akter F, Ishikawa H (2014) Synoptic features and environmental conditions of the tornado outbreak on March 22, 2013 at Brahmanbaria in the east-central region of Bangladesh. Nat Hazards 74:1309–1326

Albright MD, Recker EE, Reed RJ, Dang R (1985) The diurnal variation of deep convection and inferred precipitation in the central tropical pacific during January February 1979. Mon Weather Rev 113:1663–1680

Bao X, Zhang F, Sun J (2011) Diurnal variations of warm-season precipitation east of the Tibetan Plateau over China. Mon Weather Rev 139:2790–2810. https://doi.org/10.1175/mwr-d-11-00006.1

Barr-Kumarakulasinghe S, Lwiza K (1998) Deep convective cloud scales and direct adjustment of upper troposphere moisture in TWP environment. Meteorol Atmos Phys 66:35–50

Byon J-Y, Lim G-H (2005) Diurnal variation of tropical convection during TOGA COARE IOP. Adv Atmos Sci 22:685–702. doi:https://doi.org/10.1007/bf02918712

Carvalho LMV, Jones C (2001) A satellite method to identify structural properties of mesoscale convective systems based on the maximum spatial correlation tracking technique (MASCOTTE). J Appl Meteorol 40:1683–1701

Chen SS, Houze RA (1997a) Diurnal variation and life-cycle of deep convective systems over the tropical Pacific warm pool. Q J R Meteorol Soc 123:357–388

Chen SS, Houze RA (1997b) Interannual variability of deep convection over the tropical warm pool. J Geophys Res Atmos 102:25783–25795

Chen TC, Takahashi K (1995) Diurnal variation of outgoing longwave radiation in the vicinity of the South China sea: effect of intraseasonal oscillation. Mon Weather Rev 123:566–577

Chen H, Rucong YU, Jian LI, Yuan W, Zhou T (2010) Why nocturnal long-duration rainfall presents an eastward-delayed diurnal phase of rainfall down the Yangtze River Valley. J Clim 23:905–917

Chen G, Iwasaki T, Qin H, Sha W (2014) Evaluation of the warm-season diurnal variability over East Asia in recent reanalyses JRA-55, ERA-Interim, NCEP CFSR, and NASA MERRA. J Clim 27:5517–5537

Chen X, Zhang F, Zhao K (2016) Diurnal variations of land/sea breeze and its related precipitation over South China. J Atmos Sci 73:4793–4815. https://doi.org/10.1175/jas-d-16-0106.1

Chen D et al (2019a) Mesoscale convective systems in the Asian monsoon region from advanced himawari imager: algorithms and preliminary results. J Geophys Res Atmos 124:2210–2234

Chen X, Zhang F, Ruppert JH Jr (2019b) Modulations of the diurnal cycle of coastal rainfall over south China caused by the boreal summer intraseasonal oscillation. J Clim 32:2089–2108. https://doi.org/10.1175/jcli-d-18-0786.1

Czernecki B, Taszarek M, Marosz M, Półrolniczak M, Kolendowicz L, Wyszogrodzki A, Szturc J (2019) Application of machine learning to large hail prediction: the importance of radar reflectivity, lightning occurrence and convective parameters derived from ERA5. Atmos Res 227:249–262

Dai A, Deser C (1999) Diurnal and semidiurnal variations in global surface wind and divergence fields. J Geophys Res Atmos 104:31109–31125

Duvel JP (1989) Convection over tropical Africa and the Atlantic Ocean during northern summer. Part I: interannual and diurnal variations. Mon Weather Rev 117:2782–2799

Feidas H, Cartalis C (2005) Application of an automated cloud-tracking algorithm on satellite imagery for tracking and monitoring small mesoscale convective cloud systems. Int J Remote Sens 26:1677–1698

Feng Z, Dong X, Xi B, Schumacher C, Minnis P, Khaiyer M (2011) Top-of-atmosphere radiation budget of convective core/stratiform rain and anvil clouds from deep convective systems. J Geophys Res Atmos 116:1–13

Feng Z, Dong X, Xi B, McFarlane SA, Kennedy A, Lin B, Minnis P (2012) Life cycle of midlatitude deep convective systems in a Lagrangian framework. J Geophys Res Atmos. https://doi.org/10.1029/2012jd018362

Fiolleau T, Roca R (2013) An algorithm for the detection and tracking of tropical mesoscale convective systems using infrared images from geostationary satellite. IEEE Trans Geosci Remote Sens 51:4302–4315

Fu R, Del Genio AD, Rossow WB (1990) Behavior of deep convective clouds in the tropical Pacific deduced from ISCCP radiances. J Clim 3:1129–1152

Garreaud RD, Wallace JM (1997) The diurnal March of convective cloudiness over the Americas. Mon Weather Rev 125:3157–3171

Hassim M, Lane T, Grabowski W (2016) The diurnal cycle of rainfall over New Guinea in convection-permitting WRF simulations. Atmos Chem Phys 16:161–175

Heikenfeld M, Marinescu PJ, Christensen M, Watson-Parris D, Stier P (2019) Tobac 1.2: towards a flexible framework for tracking and analysis of clouds in diverse datasets. Geosci Model Dev 12:4551–4570

Hennermann K, Berrisford P (2018) What are the changes from ERA-Interim to ERA5. European Centre for Medium-Range Weather Forecasts

Hersbach H, Dee D (2016) ERA5 reanalysis is in production, ECMWF Newsletter. Available at http://www.ecmwf.int/sites/default/files/elibrary/2016/16299-newsletter-no147-spring-2016.pdf. Accessed 21 Aug 2019

Ho C-H, Park M-S, Choi Y-S, Takayabu YN (2008) Relationship between intraseasonal oscillation and diurnal variation of summer rainfall over the South China Sea. Geophys Res Lett 35:1–6

Hodges KI, Thorncroft CD (1997) Distribution and statistics of African mesoscale convective weather systems based on the ISCCP Meteosat imagery. Mon Weather Rev 125:2821–2837

Houze RA Jr (2004) Mesoscale convective systems. Rev Geophys. https://doi.org/10.1029/2004rg000150

Houze RA, Geotis SG Jr, West FDM (1981) Winter monsoon convection in the vicinity of North Borneo. Part I: structure and time variation of the clouds and precipitation. Mon Weather Rev 109:1595–1614. https://doi.org/10.1175/1520-0493(1981)109%3c1595:wmcitv%3e2.0.co;2

Huang WR, Chan JCL (2011) Maintenance mechanisms for the early-morning maximum summer rainfall over southeast China. Q J R Meteorol Soc 137:959–968

Huang WR, Hsu HH, Wang SY, Chen JP (2015) Impact of atmospheric changes on the low-frequency variations of convective afternoon rainfall activity over Taiwan. J Geophys Res Atmos 120:8743–8758

Huang W-R, Chang Y-H, Hsu H-H, Cheng C-T, Tu C-Y (2016) Summer convective afternoon rainfall simulation and projection using WRF driven by global climate model. Part II: over South China and Luzon. Terr Atmos Ocean Sci 27:673–685

Huang X, Hu C, Huang X, Chu Y, Tseng Y-h, Zhang GJ, Lin Y (2018) A long-term tropical mesoscale convective systems dataset based on a novel objective automatic tracking algorithm. Clim Dyn. doi:https://doi.org/10.1007/s00382-018-4071-0

Huffman GJ et al (2018) Algorithm theoretical basis document (ATBD) Version 4.5: NASA Global Precipitation Measurement (GPM) Integrated Multi-satellitE Retrievals for GPM (IMERG). NASA, Greenbelt

Inoue T, Vila D, Rajendran K, Hamada A, Wu X, Machado LA (2009) Life cycle of deep convective systems over the eastern tropical Pacific observed by TRMM and GOES-W. J Meteorol Soc Jpn Ser II 87:381–391

Ishimoto H, Masuda K, Mano Y, Orikasa N, Uchiyama A (2012) Irregularly shaped ice aggregates in optical modeling of convectively generated ice clouds. J Quant Spectrosc Radiat Transfer 113:632–643

Jiang Z, Zhang D-L, Xia R, Qian T (2017) Diurnal variations of presummer rainfall over Southern China. J Clim 30:755–773. https://doi.org/10.1175/jcli-d-15-0666.1

Johnson JT, Mackeen PL, Witt A, Mitchell EDW, Stumpf GJ, Eilts MD, Thomas KW (1998) The storm cell identification and tracking algorithm: an enhanced WSR-88D algorithm. Weather Forecast 13:263–276

Kawamoto K, Nakajima T, Nakajima TY (2001) A global determination of cloud microphysics with AVHRR remote sensing. J Clim 14:2054–2068

Kikuchi M, Suzuki K (2019) Characterizing vertical particle structure of precipitating cloud system from multiplatform measurements of A-train constellation. Geophys Res Lett 46:1040–1048

Kobayashi S et al (2015) The JRA-55 reanalysis: general specifications and basic characteristics. J Meteorol Soc Jpn Ser II 93:5–48

Krishnamurti TN, Kishtawal CM (2000) A pronounced continental-scale diurnal mode of the Asian summer monsoon. Mon Weather Rev 128:462–473

Lai R, Teng S, Yi B, Letu H, Min M, Tang S, Liu C (2019) Comparison of cloud properties from Himawari-8 and FengYun-4A geostationary satellite radiometers with MODIS cloud retrievals. Remote Sens 11:1703

Letu H et al (2018) Ice cloud properties from Himawari-8/AHI Next-generation geostationary satellite: capability of the AHI to monitor the DC cloud generation process. IEEE Trans Geosci Remote Sens. https://doi.org/10.1109/tgrs.2018.2882803

Li W, Luo C, Wang D, Lei T (2010) Diurnal variations of precipitation over the South China Sea. Meteorol Atmos Phys 109:33–46

Liu C, Zipser EJ, Cecil DJ, Nesbitt SW, Sherwood S (2008) A cloud and precipitation feature database from nine years of TRMM observations. J Appl Meteorol Climatol 47:2712–2728

Loeb NG, Davies R (1996) Observational evidence of plane parallel model biases: apparent dependence of cloud optical depth on solar zenith angle. J Geophys Res Atmos 101:1621–1634

Love BS, Matthews AJ, Lister GM (2011) The diurnal cycle of precipitation over the Maritime Continent in a high-resolution atmospheric model. Q J R Meteorol Soc 137:934–947

Mao JY, Wu GX (2012) Diurnal variations of summer precipitation over the Asian monsoon region as revealed by TRMM satellite data. Sci China Earth Sci 55:554–566

Mapes BE, Houze RA Jr (1993) Cloud clusters and superclusters over the oceanic warm pool. Mon Weather Rev 121:1398–1416

Mapes BE, Warner TT, Xu M (2003) Diurnal patterns of rainfall in northwestern South America. Part III: diurnal gravity waves and nocturnal convection offshore. Mon Weather Rev 131:830–844

Masunaga H (2013) A satellite study of tropical moist convection and environmental variability: a moisture and thermal budget analysis. J Atmos Sci 70:2443–2466. https://doi.org/10.1175/jas-d-12-0273.1

Mcgarry MM, Reed RJ (1978) Diurnal variations in convective activity and precipitation during phases II and III of GATE. Mon Weather Rev 106:255–267

Meneguz E, Wells H, Turp D (2016) An automated system to quantify aircraft encounters with convectively induced turbulence over Europe and the Northeast Atlantic. J Appl Meteorol Climatol 55:1077–1089

Meyer F, Beucher S (1990) Morphological segmentation. J Vis Commun Image Represent 1:21–46

Mori S et al (2004) Diurnal land–sea rainfall peak migration over Sumatera Island, Indonesian Maritime Continent, observed by TRMM satellite and intensive rawinsonde soundings. Mon Weather Rev 132:2021–2039

Nakajima TY, Nakajma T (1995) Wide-area determination of cloud microphysical properties from NOAA AVHRR measurements for FIRE and ASTEX regions. J Atmos Sci 52:4043–4059

Nitta T, Sekine S (1994) Diurnal variation of convective activity over the tropical western Pacific. J Meteorol Soc Jpn Ser II 72:627–641

Okamura R, Iwabuchi H, Schmidt KS (2017) Feasibility study of multi-pixel retrieval of optical thickness and droplet effective radius of inhomogeneous clouds using deep learning. Atmos Meas Tech 10:4747–4759. https://doi.org/10.5194/amt-10-4747-2017

Park M-S, Ho C-H, Kim J, Elsberry RL (2010) Diurnal circulations and their multi-scale interaction leading to rainfall over the South China Sea upstream of the Philippines during intraseasonal monsoon westerly wind bursts. Clim Dyn 37:1483–1499. doi:https://doi.org/10.1007/s00382-010-0922-z

Payne SW, Mcgarry MM (1977) The relationship of satellite inferred convective activity to easterly waves over West Africa and the adjacent Ocean during phase III of GATE. Mon Weather Rev 105:413–420

Phadtare J, Bhat G (2019) Characteristics of deep cloud-systems under weak and strong synoptic forcing during indian summer monsoon season. Mon Weather Rev 147:3741–3758

Purbantoro B, Aminuddin J, Manago N, Toyoshima K, Lagrosas N, Sumantyo JTS, Kuze H (2018) Comparison of cloud type classification with split window algorithm based on different infrared band combinations of Himawari-8 satellite. Adv Remote Sens 7:218

Putri NS, Hayasaka T, Whitehall KD (2017) The properties of mesoscale convective systems in indonesia detected using the grab 'Em Tag 'Em Graph 'Em (GTG) algorithm. J Meteorol Soc Jpn Ser II 95:391–409

Putri NS, Iwabuchi H, Hayasaka T (2018) Evolution of mesoscale convective system properties as derived from Himawari-8 high resolution data analyses. J Meteorol Soc Japan Ser II 96B:239–250

Ramage CS (1952) Diurnal variation of summer rainfall over East China, Korea and Japan. J Meteorol 9:83–86

Ramanathan V, Boer E (1997) A Lagrangian approach for deriving cloud characteristics from satellite observations and its implication to cloud parameterization. J Geophys Res Atmos 102:21383–21399

Rickenbach TM (1998) Cloud-top evolution of tropical oceanic squall lines from radar reflectivity and infrared satellite data. Mon Weather Rev 127:2951–2976

Rickenbach TM, Rutledge SA (1998) Convection in TOGA COARE: horizontal scale, morphology, and rainfall production. J Atmos Sci 55:2715–2729. https://doi.org/10.1175/1520-0469(1998)055%3c2715:citchs%3e2.0.co;2

Riley Dellaripa EM, Maloney ED, Toms BA, Saleeby SM, van den Heever SC (2020) Topographic effects on the Luzon diurnal cycle during the BSISO. J Atmos Sci 77:3–30

Roca R et al (2010) On the water and energy cycles in the tropics. CR Geosci 342:390–402

Ronald S, Dong X, Xi B, Feng Z, Kuligowski RJ (2016) Improving satellite quantitative precipitation estimates using GOES-retrieved cloud optical depth. J Hydrometeorol 17:557–570

Rossow WB, Schiffer RA (1999) Advances in understanding clouds from ISCCP. Bull Am Meteorol Soc 80:2261–2288

Roy SS, Balling RC Jr (2005) Analysis of diurnal patterns in winter precipitation across the conterminous United States. Mon Weather Rev 133:707–711

Shang H et al (2018) Diurnal cycle and seasonal variation of cloud cover over the Tibetan Plateau as determined from Himawari-8 new-generation geostationary satellite data. Sci Rep 8:1105

Shen L, Zhao C, Ma Z, Li Z, Li J, Wang K (2019) Observed decrease of summer sea–land breeze in Shanghai from 1994 to 2014 and its association with urbanization. Atmos Res 227:198–209

Sieglaff JM, Hartung DC, Feltz WF, Cronce LM, Lakshmanan V (2013) A satellite-based convective cloud object tracking and multipurpose data fusion tool with application to developing convection. J Atmos Ocean Technol 30:510–525. https://doi.org/10.1175/jtech-d-12-00114.1

Simpson M, Warrior H, Raman S, Aswathanarayana P, Mohanty U, Suresh R (2007) Sea-breeze-initiated rainfall over the east coast of India during the Indian southwest monsoon. Nat Hazards 42:401–413

Stenz R, Dong X, Xi B, Feng Z, Kuligowski RJ (2016) Improving satellite quantitative precipitation estimation using GOES-retrieved cloud optical depth. J Hydrometeorol 17:557–570. https://doi.org/10.1175/jhm-d-15-0057.1

Sugimoto T (1996) Kashmir 3D for 3DCG & GPS. User's Manual. 20.2 Calculation Formula (2) Hybeny's Distance Formula. http://www.kashmir3d.com/kash/manual-e/std_siki.htm. Accessed 10 Aug 2019

Sui CH, Lau KM, Takayabu YN, Short DA (1997) Diurnal variations in tropical oceanic cumulus convection during TOGA COARE. J Atmos Sci 54:639–655

Ukkonen P, Mäkelä A (2019) Evaluation of machine learning classifiers for predicting deep convection. J Adv Model Earth Syst 11:1784–1802

Umakanth N, Satyanarayana GC, Simon B, Rao M, Babu NR (2019) Inluence of convective weather related parameters on rainfall over Virajpet region on 26 April 2013. J Crit Rev 6:487–490

Wexler R (1983) Relative frequency and diurnal variation of high cold clouds in the tropical Atlantic and Pacific. Mon Weather Rev 111:1300–1304

Whitehall K et al (2014) Exploring a graph theory based algorithm for automated identification and characterization of large mesoscale convective systems in satellite datasets. Earth Sci Inf 8:663–675. doi:https://doi.org/10.1007/s12145-014-0181-3

Williams M, Houze RA (1987) Satellite-observed characteristics of winter monsoon cloud clusters. Mon Weather Rev 115:505–519

Wylie DP, Woolf HM (2000) The diurnal cycle of upper-tropospheric clouds measured by GOES-VAS and the ISCCP. Mon Weather Rev 130:171–179

Xie S-P, Xu H, Saji NH, Wang Y, Liu WT (2006) Role of narrow mountains in large-scale organization of Asian monsoon convection. J Clim 19:3420–3429. https://doi.org/10.1175/jcli3777.1

Yan JY, Liu JM, Jiang GR, Liu YJ, Yao HD (2007) Advances in the study of air–sea flux exchange over the south China Sea. Adv Earth Sci 22:685–697

Yang GY, Slingo J (2000) The diurnal cycle in the tropics. Mon Weather Rev 129:784–801

Yang S, Smith EA, Yang S, Smith EA (2006) Mechanisms for diurnal variability of global tropical rainfall observed from TRMM. J Clim 19:5190–5226

Yu CK, Jou JD (2005) Radar observations of the diurnally forced offshore convective lines along the Southeastern Coast of Taiwan. Mon Weather Rev 133:1613–1636

Yu R, Xu Y, Zhou T, Jian L (2007) Relation between rainfall duration and diurnal cycle in the warm season precipitation over central eastern China. Geophys Res Lett 34:173–180

Yuan J, Houze RA Jr (2010) Global variability of mesoscale convective system anvil structure from A-Train satellite data. J Clim 23:5864–5888

Zhou Y, Wu T (2019) Composite analysis of precipitation intensity and distribution characteristics of western track landfall typhoons over China under strong and weak monsoon conditions. Atmos Res 225:131–143